Constraints on the Spatial Distribution of Lunar Crustal Magnetic Sources From Orbital Magnetic Field Data

Joana S Oliveira, Foteini Vervelidou, Mark A Wieczorek, Marina Díaz Michelena

JGR Planets

RESEARCH ARTICLE
10.1029/2023JE008125

Constraints on the Spatial Distribution of Lunar Crustal Magnetic Sources From Orbital Magnetic Field Data

Joana S. Oliveira[1,2], Foteini Vervelidou[3], Mark A. Wieczorek[3], and Marina Díaz Michelena[1]

[1]Space Magnetism Area, Payloads and Space Sciences Department, National Institute of Aerospace Technology, Torrejón de Ardoz, Spain, [2]Telespazio UK SL for ESA, European Space Astronomy Centre (ESAC), Madrid, Spain, [3]Institut de Physique du Globe de Paris, CNRS, Université Paris Cité, Paris, France

Key Points:

- We test the performance of Parker's method in retrieving the surface projection of the subsurface distribution of magnetized materials
- We find that this method successfully retrieves the surface projection of typical crustal magnetic sources
- We investigate the origin of two prominent lunar magnetic anomalies: Reiner Gamma and the Mendel-Rydberg impact basin

Supporting Information:

Supporting Information may be found in the online version of this article.

Correspondence to:

J. S. Oliveira,
joana.oliveira@ext.esa.int

Citation:

Oliveira, J. S., Vervelidou, F., Wieczorek, M. A., & Díaz Michelena, M. (2024). Constraints on the spatial distribution of lunar crustal magnetic sources from orbital magnetic field data. *Journal of Geophysical Research: Planets*, *129*, e2023JE008125. https://doi.org/10.1029/2023JE008125

Received 3 OCT 2023
Accepted 29 JAN 2024

Author Contributions:

Conceptualization: Joana S. Oliveira, Foteini Vervelidou
Formal analysis: Joana S. Oliveira, Foteini Vervelidou
Funding acquisition: Joana S. Oliveira
Investigation: Joana S. Oliveira
Methodology: Joana S. Oliveira
Software: Joana S. Oliveira
Validation: Foteini Vervelidou
Visualization: Joana S. Oliveira
Writing – original draft: Joana S. Oliveira, Foteini Vervelidou, Mark A. Wieczorek
Writing – review & editing: Joana S. Oliveira, Foteini Vervelidou, Mark A. Wieczorek, Marina Díaz Michelena

Abstract Spacecraft measurements show that the crust of the Moon is heterogeneously magnetized. The sources of these magnetic anomalies are yet not fully understood, with most not being related to known geological structures or processes. Here, we use an inversion methodology that relies on the assumption of unidirectional magnetization, commonly referred to as Parker's method, to elucidate the origin of the magnetic sources by constraining the location and geometry of the underlying magnetization. This method has been used previously to infer the direction of the underlying magnetization but it has not been tested as to whether it can infer the geometry of the source. The performance of the method is here assessed by conducting a variety of tests, using synthetic magnetized bodies of different geometries mimicking the main geological structures potentially magnetized within the lunar crust. Results from our tests show that this method successfully localizes and delineates the two-dimensional surface projection of subsurface three-dimensional magnetized bodies, provided their magnetization is close to unidirectional and the magnetic field data are of sufficient spatial resolution and reasonable signal-to-noise ratio. We applied this inversion method to two different lunar magnetic anomalies, the Mendel-Rydberg impact basin and the Reiner Gamma swirl. For Mendel-Rydberg, our analysis shows that the strongest magnetic sources are located within the basin's inner ring, whereas for Reiner Gamma, the strongest magnetic sources form a narrow dike-like body that emanates from the center of the Marius Hills volcanic complex.

Plain Language Summary Magnetometers onboard spacecraft have detected magnetic field signals originating from the lunar crust. These signals are known as magnetic anomalies and are generated by rocks that are permanently magnetized. Lunar magnetic anomalies are distributed heterogeneously over the lunar surface and the geological processes that gave rise to them is under debate. By inferring the shape of the underlying magnetized material, we can constrain these processes and shed light on the Moon's geological history. In this study, we evaluate the ability of a methodology up to now used to infer the direction of the magnetization, to recover the location and shape of the magnetized material. Through a series of tests, we show that this method can constrain the shape of the source of a magnetic anomaly, provided that the respective part of the crust is magnetized along a common direction. We then apply the method to two lunar magnetic anomalies. The inferred shape and location are in good agreement with the associated geological features and suggest that one originated by an impact event and the other by volcanic activity. Future applications can focus on constraining the origin of the many lunar magnetic anomalies that are not associated with visible geological features.

1. Introduction

Orbital spacecraft and ground magnetic field observations, together with paleomagnetic analysis of Apollo samples, have demonstrated that the crust of the Moon is, at least, partially magnetized (Fuller & Cisowski, 1987; Hood et al., 1981; Lin, 1979; Mitchell et al., 2008; Purucker, 2008; Purucker & Nicholas, 2010; Richmond & Hood, 2008; Takahashi et al., 2014; Tsunakawa et al., 2015). Magnetic anomalies, and the corresponding magnetization in the crust, are found to be heterogeneously distributed over the lunar surface (Carley et al., 2012; Richmond & Hood, 2008; Tsunakawa et al., 2015; Wieczorek, 2018). However, the origin of lunar crustal magnetism is still not fully understood (for a review, see Wieczorek et al. (2022)). One of the reasons is that the Apollo samples are derived from a small number of geologic units that formed over a restricted range in time on the lunar nearside hemisphere. Another reason is that magnetic anomalies related to prominent geological features, like impact basins and albedo anomalies, have received the most attention by the scientific community (Garrick-Bethell & Kelley, 2019; Hemingway & Garrick-Bethell, 2012; Hood & Schubert, 1980). This precludes

a deep understanding of most of the geological processes associated to the sources of lunar magnetic anomalies, as most of them are not found to correlate with topography, surface geology, or gravity.

Nevertheless, lunar magnetic anomalies have a great potential to be used as a tool to understand lunar geologic history. For a magnetic anomaly to be formed, a combination of several factors must be met, namely (a) the availability of magnetic carriers, (b) the presence of an ambient magnetic field, and (c) a geological mechanism that allows the magnetic carriers to acquire magnetization. The main magnetic carriers in lunar rocks are the metallic iron-nickel minerals kamacite, martensite and schreibersite. While most lunar rocks are poor in single-domain magnetic carriers (i.e., the most ideal magnetic recorders), they do have magnetic carriers that lie in the vortex state, and are therefore capable of preserving their magnetization over billions of years (Wieczorek et al., 2022). Concerning the presence of an ambient magnetic field, the Moon has currently no internally generated global magnetic field but it is believed to have once had a magnetic field in its past that could have magnetized the lunar crust. Currently, the most widely accepted hypothesis for the origin of a magnetizing field is that a dynamo once operated in the Moon's metallic core (Dwyer et al., 2011; Laneuville et al., 2014, 2018; Le Bars et al., 2011; Scheinberg et al., 2015). Alternatively, transient fields generated by impact events have also been proposed to be responsible for magnetizing lunar rocks (Hood & Artemieva, 2008; Tarduno et al., 2021). However, recent magnetohydrodynamic and impact simulations have shown that this mechanism cannot generate the required field strengths, leaving a core dynamo as the most probable explanation (Oran et al., 2020).

As far as geological mechanisms are concerned that would allow the magnetic carriers to acquire magnetization, given that the lunar surface is highly cratered, a plausible explanation for a certain number of magnetic anomalies is that their origin is related to impact events. Impacts heat the crust locally above the Curie temperature, and as these materials cooled, they could have acquired a thermoremanent magnetization if there was an ambient field present (Hood, 2011; Wieczorek et al., 2012). Moreover, impacts enrich the metal-poor lunar crust with iron-rich materials derived from the impactor. Impact events can therefore lead to magnetic anomalies that are related to shallow geological structures that are either apparent (craters, basins, ejecta) or subsurface (resurfaced craters and basins). Other geological mechanisms that could generate a magnetic anomaly are volcanic and magmatic activity (Hemingway & Tikoo, 2018; Purucker et al., 2012). These processes give rise to either shallow or deep geological features, such as domes, dikes, magmatic chambers, and lava tubes. Magmatic activity can also produce strong magnetic carriers by thermochemically altering lunar rocks (Hemingway & Tikoo, 2018). Moreover, the primordial crust of the Moon could have become magnetized as it cooled in the first 100 million years of lunar history (Wieczorek, 2018). Parts of this primordial magnetization might still be present in the deep lunar crust. From the above considerations, it is evident that the mechanisms that gave rise to the magnetic anomalies are closely linked to the geological processes that have shaped both the interior and the surface of the Moon, such as the thermal evolution of the lunar mantle and core (Arkani-Hamed & Boutin, 2014; Hood, 2011; Maxwell & Garrick-Bethell, 2020; Nayak et al., 2017; Oliveira & Wieczorek, 2017), the geological history of its surface (Hood, Torres, et al., 2021), and the deposition of iron-rich material by impactors (Oliveira et al., 2017; Wieczorek et al., 2012).

Previous studies have attempted to constrain the magnetization underlying the magnetic anomalies by relying on available regional geological context, like associated albedo anomalies, also known as swirls (Garrick-Bethell & Kelley, 2019; Hemingway & Tikoo, 2018; Hood & Schubert, 1980), topography (Oliveira et al., 2017), and gravity (Gong & Wieczorek, 2020; Kelley & Garrick-Bethell, 2020). Swirls are always associated with magnetic anomalies and are thought to be the result of the crust being locally shielded from the solar wind by the crustal magnetic field. Reiner Gamma is the most prominent swirl (Hood & Schubert, 1980) and it has been used to constrain the geometry, magnetization and origin of the associated magnetic source (e.g., Garrick-Bethell & Kelley, 2019; Hemingway & Tikoo, 2018). The topography can give information about the distribution of shallow magnetic sources such as impact melt sheets and ejecta. Oliveira et al. (2017) used topography to infer the magnetization of impact melt sheets within large impact basins and consequently to constrain the metal iron abundance in the melt sheet. Gravity can be used to locate dense, iron-rich bodies that lie deep in the crust. Kelley and Garrick-Bethell (2020) used gravity information to interpret a magnetic anomaly close to Marius Hills as linked to an old impact crater that was later filled by volcanic material. However, in order to study the large number of magnetic anomalies that are neither associated with swirls nor correlated with topography and gravity, a methodology is needed that does not rely heavily on available geological or geophysical context.

Here we propose to use the inversion method of Parker (1991) to constrain the spatial distribution of magnetization within the lunar crust. It was originally designed to infer the magnetization direction of seamounts on Earth and has been shown to accurately retrieve the magnetization direction when the magnetized sources are unidirectional, without making any assumptions about the geometry of the sources (Parker, 1991). It has been applied previously to various planetary bodies in order to infer the orientation and geometry of ancient core dynamo magnetic fields (Oliveira & Wieczorek, 2017; Oliveira et al., 2019; Thomas et al., 2018). Moreover, Oliveira et al. (2017) used Parker's method to infer the iron abundances within lunar basins, by combining the inferred magnetization distribution within the basins' inner depression with estimates of the thickness and geometry of the central impact melt sheet. However, the ability of the method to constrain the spatial distribution of subsurface magnetization without any a priori information about either its location or geometry has not been assessed up to now.

In this work, we test the performance of Parker's method by applying it to synthetic magnetic field data sets, generated from a variety of geologically plausible three-dimensional magnetized bodies. The paper is structured as follows. In the methodology section, Section 2, we present Parker's inversion methodology, and how we constructed the synthetic data sets. In Section 3, we present and discuss the results we obtained from these synthetic tests. In Section 4, we apply the method to two prominent lunar magnetic anomalies associated with surface geological features: the magnetic anomaly over the Mendel-Rydberg impact basin, and the magnetic anomaly over Reiner gamma, a swirl albedo marking, which is the target of the upcoming Lunar Vertex mission (Blewett et al., 2022). In Section 5, we summarize our results and present our conclusions.

2. Methods

2.1. Inversion Methodology

The inversion method of Parker (1991), hereafter referred to as Parker's method, is a least squares inversion technique that allows estimation of the strength and location of a set of magnetic dipoles, all pointing in the same direction, that best fits a local set of magnetic field data. The underlying magnetization is considered as an ensemble of dipoles lying within the magnetized volume. By assuming that the magnetization is unidirectional, Parker (1991) demonstrated that this volumetric distribution of dipoles is equivalent to dipoles placed only on the surface and pointing in the same direction. The discrete distribution of surface dipole moments can be described by the following equation:

$$\mathbf{M}(\mathbf{s}_i) = \hat{\mathbf{m}}\, m(\mathbf{s}_i), \qquad m(\mathbf{s}_i) \geq 0, \tag{1}$$

where $\hat{\mathbf{m}}$ is the direction vector, m is the magnitude of the dipole moment, and $\mathbf{s}_i$ is the position vector.

Parker (1991) analyzed only the component aligned with Earth's global magnetic field. Given the absence of a core magnetic field on the Moon, we follow previous lunar applications (Oliveira & Wieczorek, 2017; Oliveira et al., 2017) and analyze only the radial magnetic field component. The radial magnetic field, d_j, at observation point j is given by the following sum

$$d_j = \sum_{i=1}^{N_d} g_j(\mathbf{s}_i)\, m(\mathbf{s}_i), \qquad j = 1, \ldots, N_{obs}, \tag{2}$$

where

$$g_j(s_i) = \frac{\mu_0}{4\pi}\left(\frac{3\hat{\mathbf{m}}\cdot(\mathbf{r}_j - \mathbf{s}_i)\;\hat{\mathbf{r}}_j\cdot(\mathbf{r}_j - \mathbf{s}_i)}{|\mathbf{r}_j - \mathbf{s}_i|^5} - \frac{\hat{\mathbf{m}}\cdot\hat{\mathbf{r}}_j}{|\mathbf{r}_j - \mathbf{s}_i|^3}\right), \tag{3}$$

with μ_0 the permeability of free space, N_{obs} the number of observations at a given (varying or constant) altitude, N_d the number of dipoles at the surface, and $\mathbf{r}_j$ the position vector of a given observation relative to a fixed origin. By combining Equations 2 and 3 into a typical matrix form, we obtain

$$\mathbf{d} = \mathbf{G}(\hat{\mathbf{m}})\, \mathbf{m}, \tag{4}$$

where **d** is the vector of the radial magnetic field observations, **m** is the vector containing the magnitude of the dipole moments (with each element greater or equal to zero), and **G**, which is a function of the magnetization direction $\hat{\mathbf{m}}$, is the matrix that contains the elements given by Equation 3.

In this study, we are interested in inferring the strength and location of dipoles with non-zero dipole moment. For this, we follow closely the protocol used in Oliveira and Wieczorek (2017) and Oliveira et al. (2017):

1. We construct an equidistant grid of dipoles within an angular radius of 8° at a given location on the lunar surface. The dipoles are placed on the surface of the selenocentric reference system, and the dipoles are distributed in an equidistant manner using the spherical distribution technique of Katanforoush and Shahshahani (2003) with an average spacing of 6 km (0.2° at the equator).
2. We consider synthetic magnetic field data distributed over a grid within an angular radius of 9°, which is slightly larger in extent than the grid of surface dipoles. These data are placed at 30 km altitude above the selenocentric reference system, and the measurements have an average angular spacing of 0.45° (13.5 km at the equator). The observation grid is chosen to be 1° larger than the grid of surface dipoles in order to avoid potential edge effects associated with the surface magnetization.
3. We use the non-negative least squares (nnls) technique developed by Lawson and Hanson (1974) to solve Equation 4 for the location and strength of the surface dipoles with non-zero dipole moment for a given magnetization direction. A property of the non-negative least squares inversion is that the number of non-zero elements in the solution vector m is always less than or equal to the number of measurements N_{obs}. By considering all magnetization directions, we then determine the direction that minimizes the root-mean-square (RMS) misfit between the radial components of the input and the modeled magnetic field. The magnetization direction is varied over an equidistant spherical grid with an angular spacing of 4°.

2.2. Synthetic Magnetic Field Observations

We tested the performance of Parker's method in locating magnetized material by generating synthetic magnetization distributions and using their resulting magnetic field as input to the inversion scheme of Parker's method. Rather than generating strictly unidirectional magnetization distributions, we consider the more realistic case of a magnetization acquired by material cooling in the presence of an internal dipolar magnetic field. In this scenario, the smaller the spatial extent of the magnetization distribution, the closer to unidirectional it is. The inversion technique was applied to various synthetic data sets derived from assumed distributions of magnetization that might mimic plausible geological structures on the Moon. Spherical caps were used to mimic melt sheets within basins, and spherical parallelepipeds, defined as parallelepipeds whose upper and lower surfaces follow the curvature of the sphere at the respective depths and whose remaining four sides converge to the center of the sphere, hereafter called parallelepipeds for brevity, were used to mimic lava tubes and dikes.

A schematic representation of these shapes is shown in Figure 1. We generated multiple magnetic field data sets from each shape by varying the magnetization direction, the depth to the top, the lateral size, and the thickness of the body. The exact values used for each of these parameters per shape are given in Table 1. It is worth noting that a given shape can represent different geological structures depending on the selected parameters. For example, a shallow spherical cap could represent a melt sheet, but if placed at deeper depths it could also mimic a magmatic laccolith.

Each source is represented as a 3D magnetization distribution, $\mathbf{M}(r',\theta',\phi')$. The magnetic field, **B**, at point $\mathbf{s} = (r,\theta,\phi)$ is calculated by estimating the integral

$$\mathbf{B}(\mathbf{s}) = -\nabla\frac{\mu_0}{4\pi}\int_{\Omega'}\mathbf{M}(\mathbf{s}')\nabla'\frac{1}{|\mathbf{s}-\mathbf{s}'|}d\Omega', \tag{5}$$

where μ_0 is the permeability of free space, Ω' is the magnetized volume, and $d\Omega'$ is the volume element $r'^2 \sin\theta' d\theta' d\phi' dr'$. Both the magnetization, **M**, and the term $\frac{1}{|\mathbf{s}-\mathbf{s}'|}$ were treated as expansions of spherical harmonic function (for details see Appendix A). For the expansion of the magnetization, we used spherical harmonics up to a maximum degree and order 800, and for the expansion of the term $\frac{1}{|\mathbf{s}-\mathbf{s}'|}$, which determines the spatial resolution of the induced magnetic field, we used spherical harmonic functions up to maximum degree and order 400. The smallest wavelength that this data set can resolve is about 0.9°, which corresponds to 27 km on the surface.

10.1029/2023JE008125

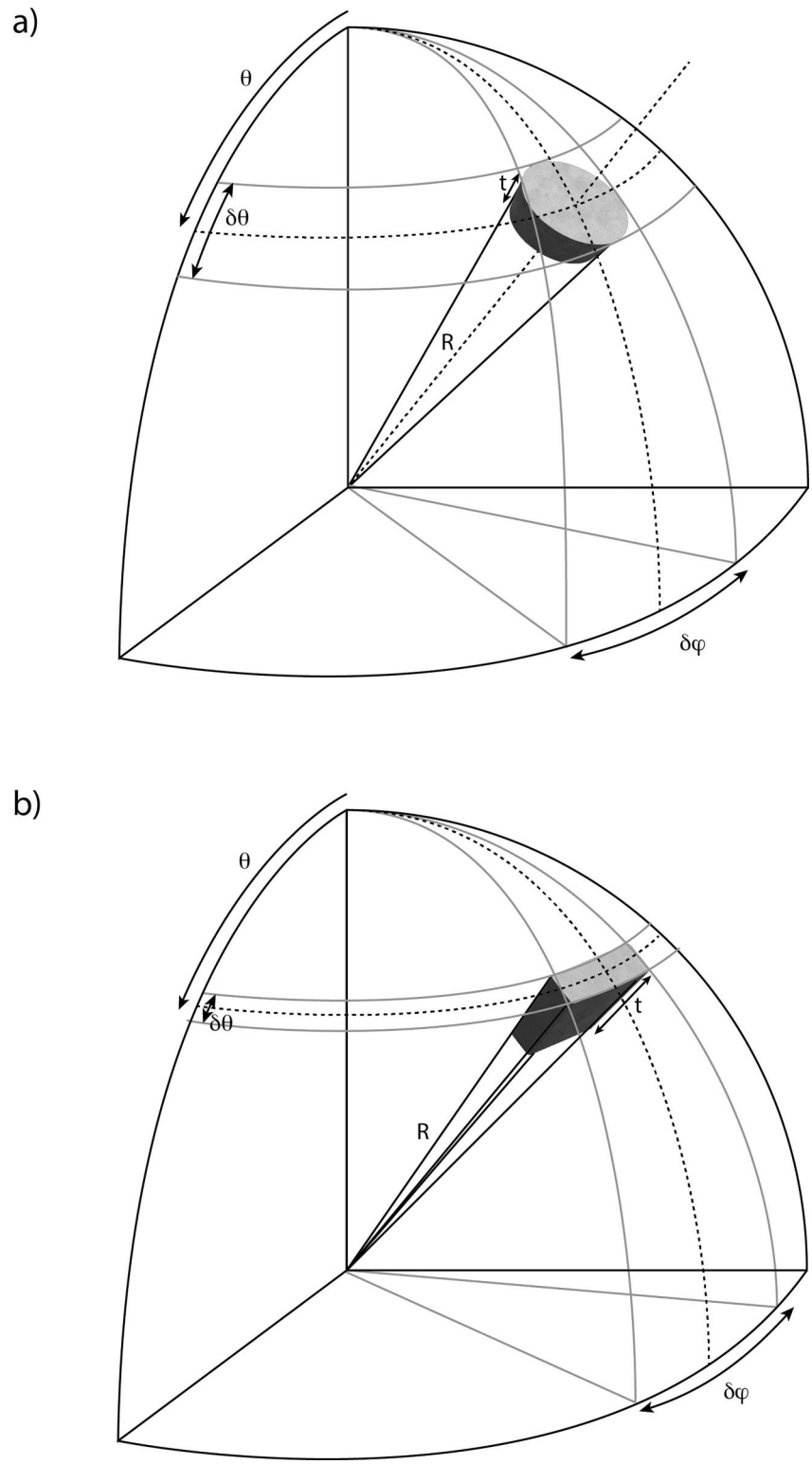

Figure 1. Schematic representation of the magnetized bodies used in our synthetic tests. (a) spherical caps and (b) parallelepipeds. t denotes the body's thickness, and $\delta\theta$ and $\delta\phi$ denote respectively the latitudinal and longitudinal angular aperture. The top surface of all three shapes corresponds to a sphere with radius R. Rectangular tubes are a special case of the parallelepiped geometry where t is equal to $0.7 \times R\delta\theta$.

Table 1
Inversion Results for the Ideal Synthetic Cases

Shape	Dimensions		$\|B_r\|^{max}$ (nT)	N	m_{min} (A m^2)	m_{max} (A m^2)	Misfit (nT)	Threshold (%)	$SM_{\%}$	$SM_{30\%}$
Spherical cap	t (km)	1	0.74	1,216	1.15×10^{6}	1.42×10^{10}	8.14×10^{-4}	58	0.98	0.95
		10	7.00	1,206	5.65×10^{4}	1.35×10^{11}	1.06×10^{-2}	56	0.98	0.95
		20	**13.17**	**1,200**	$\mathbf{1.77 \times 10^{7}}$	$\mathbf{2.54 \times 10^{11}}$	$\mathbf{2.67 \times 10^{-2}}$	**56**	**0.97**	**0.93**
		30	18.58	1,197	3.23×10^{7}	3.60×10^{11}	4.83×10^{-2}	55	0.98	0.92
		40	23.27	1,196	1.17×10^{8}	4.53×10^{11}	7.53×10^{-2}	55	0.97	0.91
	d (km)	1	14.78	1,221	1.51×10^{5}	2.83×10^{11}	1.67×10^{-2}	59	0.98	0.96
		10	**13.17**	**1,200**	$\mathbf{1.77 \times 10^{7}}$	$\mathbf{2.54 \times 10^{11}}$	$\mathbf{2.67 \times 10^{-2}}$	**56**	**0.97**	**0.93**
		20	11.55	1,195	9.12×10^{6}	2.26×10^{11}	3.93×10^{-2}	57	0.97	0.89
		30	10.05	1,194	2.03×10^{7}	2.00×10^{11}	5.13×10^{-2}	58	0.96	0.86
		40	8.71	1,189	1.06×10^{8}	1.76×10^{11}	6.38×10^{-2}	59	0.96	0.82
	$\delta\phi$ (°)	2	10.84	1,188	3.83×10^{6}	1.55×10^{11}	2.45×10^{-3}	56	1	0.98
		6	**13.17**	**1,200**	$\mathbf{1.77 \times 10^{7}}$	$\mathbf{2.54 \times 10^{11}}$	$\mathbf{2.67 \times 10^{-2}}$	**56**	**0.97**	**0.93**
		10	10.84	1,218	7.00×10^{8}	2.67×10^{11}	1.11×10^{-1}	65	0.97	0.70
	α (°)	**0**	**13.17**	**1,200**	$\mathbf{1.77 \times 10^{7}}$	$\mathbf{2.54 \times 10^{11}}$	$\mathbf{2.67 \times 10^{-2}}$	**56**	**0.97**	**0.93**
		45	10.44	1,223	2.21×10^{6}	1.98×10^{11}	1.74×10^{-2}	55	0.99	0.93
		90	4.54	1,298	1.55×10^{7}	1.19×10^{11}	1.83×10^{-2}	57	1	0.93
		135	10.44	1,195	2.76×10^{7}	1.99×10^{11}	1.82×10^{-2}	54	1	0.93
		180	13.17	1,200	1.77×10^{7}	2.54×10^{11}	2.67×10^{-2}	56	0.97	0.93
Parallelopiped[a]	t (km)	1	0.25	1,093	2.97×10^{4}	5.91×10^{9}	3.82×10^{-5}	70	1	0.98
		10	2.06	1,178	6.85×10^{4}	4.50×10^{10}	4.93×10^{-4}	77	0.78	0.97
		20	3.44	1,197	8.81×10^{5}	7.16×10^{10}	1.26×10^{-3}	80	0.78	0.97
		30	**4.40**	**1,195**	$\mathbf{3.81 \times 10^{6}}$	$\mathbf{8.95 \times 10^{10}}$	$\mathbf{2.30 \times 10^{-3}}$	**83**	**0.78**	**0.96**
		40	5.11	1,193	1.92×10^{6}	1.03×10^{11}	3.62×10^{-3}	84	0.78	0.96
	d (km)	1	6.50	1,099	1.51×10^{6}	1.57×10^{11}	1.57×10^{-3}	68	1	0.98
		10	**4.40**	**1,195**	$\mathbf{3.81 \times 10^{6}}$	$\mathbf{8.95 \times 10^{10}}$	$\mathbf{2.30 \times 10^{-3}}$	**83**	**0.78**	**0.96**
		20	3.02	1,185	1.04×10^{6}	5.69×10^{10}	3.16×10^{-3}	91	0.56	0.93
		30	2.16	1,186	1.58×10^{7}	3.98×10^{10}	4.00×10^{-3}	94	0.33	0.9
		40	1.62	1,185	$6.78E \times 10^{5}$	3.00×10^{10}	5.04×10^{-3}	96	0.33	0.87
	$\delta\theta$ (°)	**0.5**	**4.40**	**1,195**	$\mathbf{3.81 \times 10^{5}}$	$\mathbf{8.95 \times 10^{10}}$	$\mathbf{2.30 \times 10^{-3}}$	**83**	**0.78**	**0.96**
		1	8.39	1,187	9.39×10^{6}	1.62×10^{11}	4.62×10^{-3}	59	0.86	0.97
		2	15.29	1,188	1.33×10^{7}	2.58×10^{11}	1.07×10^{-2}	72	0.74	0.96
		3	17.99	1,187	7.04×10^{7}	3.03×10^{11}	1.67×10^{-2}	53	0.94	0.96
		4	18.64	1,193	6.01×10^{6}	3.20×10^{11}	2.21×10^{-2}	58	0.95	0.95
	α (°)	**0**	**4.40**	**1,195**	$\mathbf{3.81 \times 10^{6}}$	$\mathbf{8.95 \times 10^{10}}$	$\mathbf{2.30 \times 10^{-3}}$	**83**	**0.78**	**0.96**
		45	3.31	1,208	3.29×10^{5}	7.05×10^{10}	1.57×10^{-3}	82	0.78	0.96
		90	1.15	1,263	9.51×10^{5}	4.53×10^{10}	2.02×10^{-3}	84	0.78	0.96
		135	3.30	1,190	5.95×10^{6}	7.06×10^{10}	1.58×10^{-3}	85	0.78	0.96
		180	4.40	1,195	3.81×10^{6}	8.95×10^{10}	2.30×10^{-3}	83	0.78	0.96
Rectangular tube[b]	d (km)	**2**	**9.52**	**1,202**	$\mathbf{1.90 \times 10^{6}}$	$\mathbf{2.01 \times 10^{11}}$	$\mathbf{2.36 \times 10^{-3}}$	**50**	**0.94**	**0.98**
		5	8.42	1,194	3.77×10^{6}	1.72×10^{11}	2.80×10^{-3}	50	0.94	0.98
		10	6.94	1,191	1.63×10^{6}	1.36×10^{11}	3.55×10^{-3}	56	0.94	0.97
		15	5.80	1,191	1.05×10^{7}	1.10×10^{11}	4.33×10^{-3}	65	0.94	0.96
		20	4.90	1,189	8.22×10^{6}	9.13×10^{10}	5.12×10^{-3}	71	0.76	0.94
	$\delta\theta$ (°)	0.5	3.16	1,146	3.46×10^{5}	9.20×10^{10}	4.25×10^{-4}	50	1	0.98
		1	**9.52**	**1,202**	$\mathbf{1.90 \times 10^{6}}$	$\mathbf{2.01 \times 10^{11}}$	$\mathbf{2.36 \times 10^{-3}}$	**50**	**0.94**	**0.98**

Table 1
Continued

Shape	Dimensions		$\|B_r\|^{max}$ (nT)	N	m_{min} (A m^2)	m_{max} (A m^2)	Misfit (nT)	Threshold (%)	$SM_{\%}$	$SM_{30\%}$
		2	24.31	1,193	5.03×10^{6}	4.12×10^{11}	1.80×10^{-2}	72	0.84	0.96
		3	34.46	1,189	7.02×10^{7}	5.96×10^{11}	5.85×10^{-2}	60	0.96	0.95
		4	41.06	1,186	4.70×10^{8}	7.40×10^{11}	1.29×10^{-1}	62	0.97	0.91
	$\delta\phi$ (°)	4	9.39	1,201	3.18×10^{5}	1.97×10^{11}	1.49×10^{-3}	43	1	0.99
		6	**9.52**	**1,202**	$\mathbf{1.90 \times 10^{6}}$	$\mathbf{2.01 \times 10^{11}}$	$\mathbf{2.36 \times 10^{-3}}$	**50**	**0.94**	**0.98**
		8	9.36	1,218	7.03×10^{4}	2.02×10^{11}	3.43×10^{-3}	45	1	0.97
		10	9.26	1,225	7.17×10^{4}	2.02×10^{11}	4.72×10^{-3}	37	1	0.97
	α (°)	**0**	**9.52**	**1,202**	$\mathbf{1.90 \times 10^{6}}$	$\mathbf{2.01 \times 10^{11}}$	$\mathbf{2.36 \times 10^{-3}}$	**50**	**0.94**	**0.98**
		45	7.21	1,191	6.86×10^{6}	1.59×10^{11}	1.51×10^{-3}	52	0.94	0.98
		90	2.79	1,173	6.58×10^{5}	1.02×10^{11}	3.90×10^{-3}	49	0.94	0.98
		135	7.19	1,195	2.54×10^{6}	1.59×10^{11}	1.53×10^{-3}	51	0.94	0.98
		180	9.52	1,202	1.90×10^{6}	2.01×10^{11}	2.36×10^{-3}	50	0.94	0.98

Note. For each test case we vary either the thickness t, the depth to the top d, the lateral size (by varying the angles $\delta\theta$ and $\delta\phi$) or the magnetization direction α, while maintaining fixed the other parameters to the values shown in bold. For each test case, we show the shape's dimensions and the maximum strength of the input radial magnetic field at 30 km altitude ($|B_r|^{max}$) and the following results from Parker's method: the number of dipoles with non-zero dipole moment N, the minimum and maximum dipole moments of the obtained magnetization distribution (m_{min} and m_{max}, respectively), and the RMS misfit between the radial components of the input and the modeled magnetic field (Misfit). Also shown is the percentage of m_{max} used as a threshold to define the retained dipoles (Threshold) and the respective success metric ($SM_{\%}$) (see text for details). The last column shows the success metric when using a threshold fixed to 30% of m_{max} ($SM_{30\%}$). [a]$\delta\phi = 5°$. [b]$t = \delta\theta$, expressed in km at 45° latitude.

We considered that the sources were magnetized as they cooled in the presence of an internal dipolar magnetic field $\mathbf{B_i}$. The magnetic moment of the internal dipole was set to 1.6×10^{21} A m^2, which gives surface fields strengths of 30 and 60 μT at the magnetic equator and poles, respectively. These values are consistent with the range of paleointensities derived from lunar samples during the high-field epoch. The thermoremanent magnetization, $\mathbf{M}$, was obtained through the relationship

$$\mathbf{M} = \frac{1}{\mu_0}\chi_{trm}\mathbf{B_i}, \tag{6}$$

where we used a value of 3×10^{-3} for the thermoremanent susceptibility χ_{trm}, which is a representative value for common lunar rock types (see Table S2 of Wieczorek et al. (2012)). B_i varies as a function of longitude and latitude throughout the magnetized body, while we ignore its variations as a function of altitude by estimating it at the middle of each magnetized body. The magnetizing dynamo field was then assumed to have disappeared after the thermoremanence was acquired.

3. Results of Synthetic Tests

3.1. Ideal Synthetic Cases

For the first set of synthetic tests, we considered the magnetic field data generated by magnetized bodies in the shape of spherical caps, and two different parallelepipeds geometries. Schematic representations (not to scale) of these bodies are given in Figure 1. For each shape, we run several tests by varying the magnetization direction at the center of the magnetized body and the body's thickness, lateral size and depth to the top, d, with $d = R_{Moon} - R$, where R_{Moon} is Moon's radius. Table 1 presents the variables of each test case. The magnetization direction is given by the angle α, which represents the angular deviation of the magnetization at the center of the magnetized body with respect to the radial position vector of the body's center. For each test using a given shape, only one parameter changes, while the rest stay equal to the values presented in bold in Table 1. For each shape, the test case with all the parameters set to the values presented in bold is hereafter referred to as the nominal case for that shape.

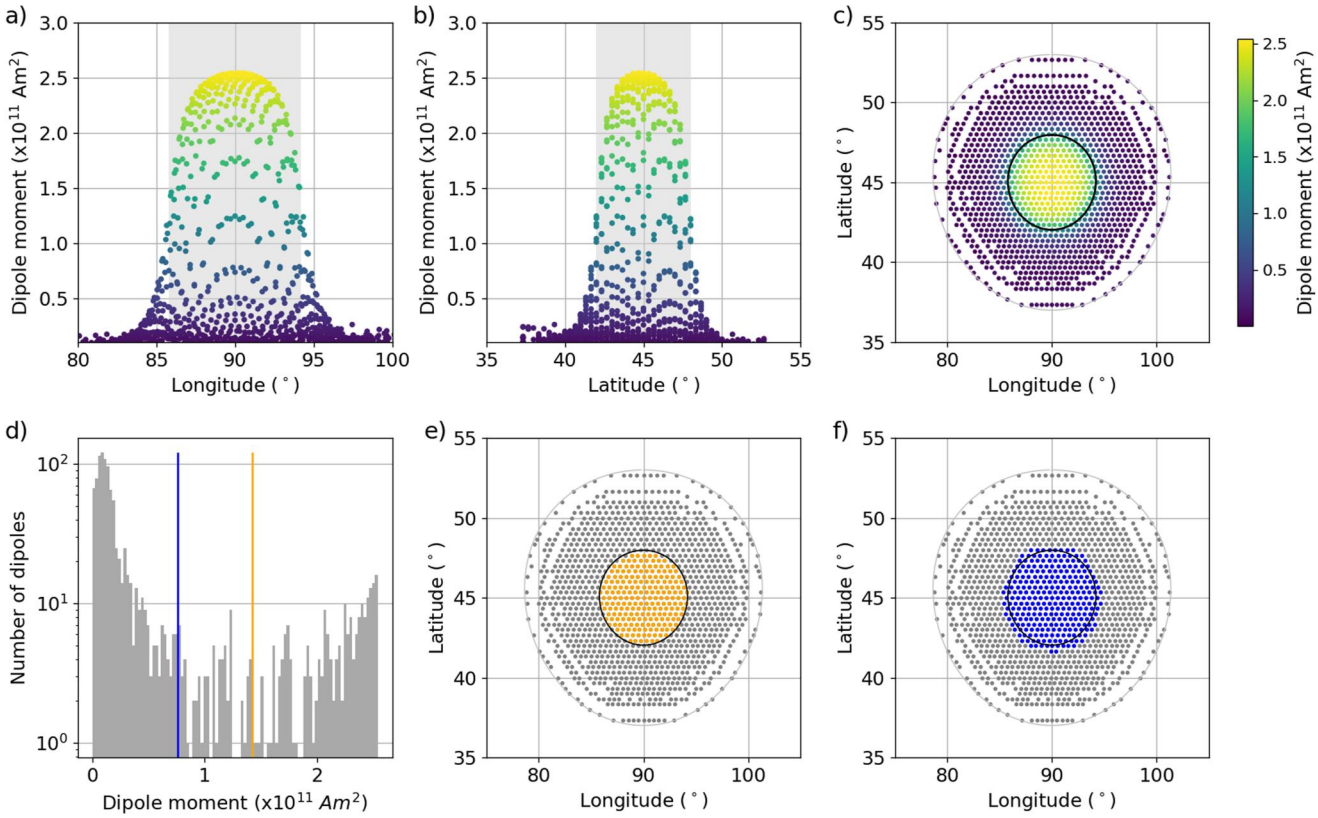

Figure 2. Inversion results of the synthetic magnetized spherical cap nominal case. The distribution of dipole moments are shown as a function of (a) longitude, (b) latitude, and (c) in two-dimensional map form. The shaded gray zones in panels (a and b) represent the surface projection of the magnetized body. (d) Histogram of the dipole moments, where the orange and blue lines denote the minimum of the dipole moments plotted in color in panels (e and f). (e) Distribution of dipoles from the inversion, where orange and gray dots lie within and outside of the surface projection of the magnetized body, respectively. (f) Same as panel (e), but only those dipoles with moments greater than 30% of the maximum dipole moment are plotted in blue. The black circle in panels (c, e, and f) delimits the surface projection of the magnetized body and the outer gray circle delimits the grid of dipoles used in the inversion.

3.1.1. Magnetized Spherical Cap

Here we present the results we obtained when considering the magnetized body to be a subsurface spherical cap, centered at 45°N latitude and 90°E longitude. Figure 2 shows the results we obtained for the nominal case (i.e., 20 km thickness, 10 km depth to the top, 6° angular aperture and $\alpha = 0°$). Figures 2a–2c show the dipole moments distribution obtained by our inversion (i.e., the magnetic moments of all dipoles assigned a non-zero dipole moment, by default positive), as a function of longitude, latitude, and in two-dimensional map form, respectively. Figure 2d shows the histogram of the dipole moment strengths. The width of each bin is 1% of the maximum dipole moment strength of the distribution of dipoles provided by the inversion, $m_{\max}$. In describing the two-dimensional extent of the magnetization from our inversion, we considered all dipole moments greater than a specified minimum value $m_{threshold}$. The threshold shown by the orange line has been chosen such that all retained dipoles fall within the surface projection of the magnetized body. The respective dipoles are shown in orange in Figure 2e. The threshold shown by the blue line has been arbitrarily chosen to be 30% of $m_{\max}$. The dipoles retained using this threshold are shown in blue in Figure 2f.

We observe that the strongest dipoles of the inversion are located inside the surface projection of the magnetized body. Both thresholds yield dipole distributions that reconstruct accurately the surface projection. Both the orange and blue points cover fully the surface projection, and the blue points that are located outside the surface projection are few and are all located close to the boundary.

Figure 3 presents the results we obtained when varying the parameters of the nominal test case. In particular, it shows histograms of the total dipole moment of all dipoles belonging in a given longitude (Figures 3a, 3c, 3e, and 3g) and latitude (Figures 3b, 3d, 3f, and 3h) range. For this, we considered bins of 1° width. Figures 3a and 3b

show the results for the various thicknesses considered (1, 10, 20, 30 and 40 km), when keeping the remaining parameters of the spherical cap the same as in Figure 2 (i.e., 10 km depth to the top, 6° angular aperture, and $\alpha = 0°$). The remaining panels of Figure 3 show the respective results when varying the depth to the top (Figures 3c and 3d), the angular aperture (Figures 3e and 3f) and the magnetization direction (Figures 3g and 3h), while keeping the remaining parameters equal to the values in bold of Table 1. When varying the depth to the top, we note that we slightly adjusted the spherical cap's angular aperture (increasing by up to 0.69°) to keep the surface projection the same for all cases and allow for a more straightforward comparison.

We observe that the central part of all the dipole moments histograms overlaps with the shaded gray zone, which marks the surface projection of the magnetized body. Moreover, as expected, the larger or thicker or shallower a magnetized body is, the larger is the sum of dipole moment strengths. The cases where the magnetization was directed upwards and downwards ($\alpha = 0°$ and $\alpha = 180°$) were found to give the same inversion results, as expected. The cases with vertical magnetization ($\alpha = 0°$ and $\alpha = 180°$) yield the strongest sum of dipole moments, while the case of horizontal magnetization ($\alpha = 90°$) is weaker by a factor of about two, as expected for a dipolar magnetizing field.

For each test case shown in Figure 3, we calculated the required threshold value such that all dipoles with equal or higher strength are located within the surface projection of the magnetized body (orange line in Figure 2d for the nominal case). The threshold values we obtained, given as a percentage of $m_{\max}$, vary for each case from 54% to 65% (see Table 1). We next tested a threshold of 30% of $m_{\max}$ (blue line in Figure 2d for the nominal case). A lower threshold of 30% is beneficial in that more dipoles are retained within the region of interest, but at the expense of retaining more that are exterior to the magnetized body. In order to evaluate the results and compare the two different threshold approaches, we defined the following success metric, SM:

$$SM = \frac{N_{ri}}{N_i} - \frac{N_{ro}}{N_o}, \tag{7}$$

where N_{ri} and N_{ro} are respectively the number of retained dipoles that lie inside and outside of the true surface projection of the magnetized body, and where N_i and N_o are the total number of dipoles with non-zero magnetic moments in the two respective regions. In order to successfully delimit the distribution of magnetization, the number of retained dipoles within the projection of the magnetized body should be similar to the total number of dipoles there, giving rise to a ratio N_{ri}/N_i close to 1. At the same time, the number of retained dipoles exterior to the projection of the magnetized body N_{ro} should be close to zero. The success metric should thus be as close to 1 as possible.

The success metric values are given in Table 1 for all test cases and for both threshold approaches: $SM_{\%}$ corresponds to the threshold, as a percentage of $m_{\max}$, that is chosen case-by-case such that the retained dipoles all fall within the surface projection of the magnetized body, and $SM_{30\%}$ corresponds to the fixed threshold of 30% of $m_{\max}$. We see that $SM_{\%}$ ranges from 0.96 to 1, while $SM_{30\%}$ varies from 0.7 to 0.98. We obtain the lowest value of $SM_{30\%}$ equal to 0.7 for the case of a 10° angular aperture, which corresponds to the largest spherical cap considered here. The second lowest value, $SM_{30\%} = 0.82$, corresponds to the case of a 40 km burial depth. Overall, for the parameters assumed here, we find that by using the fixed threshold of 30% of $m_{\max}$, we are able to reconstruct the surface projection of the magnetized body with SM $\geq$ 0.7.

3.1.2. Magnetized Parallelepiped

Here we present the results we obtained when considering the magnetized body to be a subsurface parallelepiped, centered at 45° latitude and 90° longitude. Figure 4 shows the results we obtained for the nominal case, which has a 30 km thickness, a 10 km depth to the top of the magnetized body, a 0.5° width (corresponding to about 15 km), and a vertical magnetization ($\alpha = 0°$). Similar to Figure 2, panels a–c show the dipole moments distribution obtained by our inversion, as a function of longitude, latitude, and in two-dimensional map form, respectively. Panel d shows the histogram of the dipole moment strengths. The orange line corresponds to the threshold such that all dipoles with equal or higher dipole moments are located within the surface projection of the magnetized body, as shown in panel e. The blue line corresponds to the threshold of 30% of $m_{\max}$, where the respective dipoles are shown in panel f.

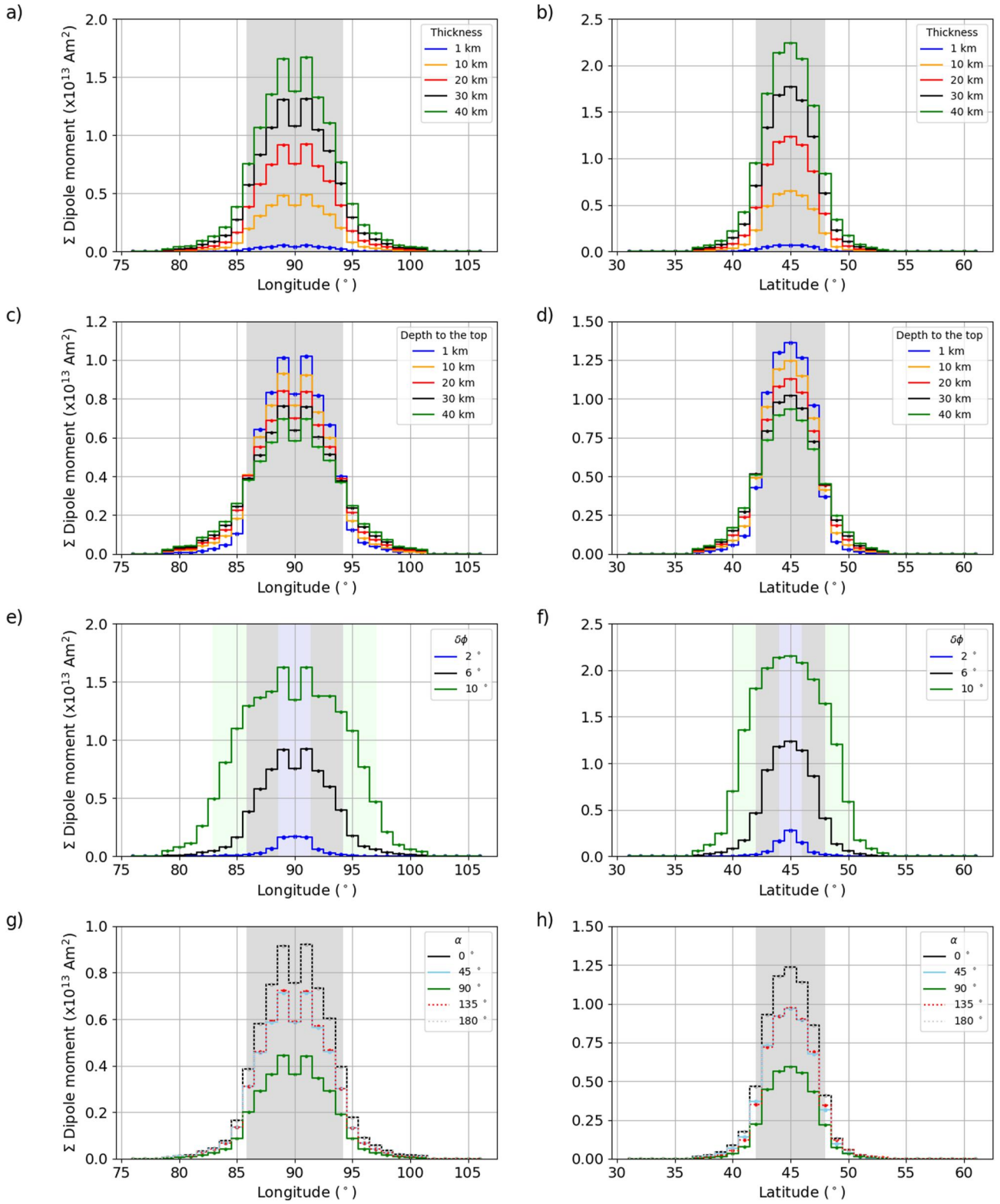

Figure 3.

We observe that the strongest dipoles are located within the surface projection of the magnetized body and cover it fully. At the same time, just as in the test case of a spherical cap, there are strong dipoles located outside of the surface projection of the magnetized body, of which most are adjacent to the boundary. By applying the first threshold (orange line in panel d), we exclude 2 out of the 9 dipoles that are located inside of the surface projection, which leads to a success metric $SM_{\%}$ of 0.78. The fixed threshold of 30% (blue line in panel d) retains all dipoles within the surface projection, but also places some dipoles outside of it. The distribution of these dipoles is such that the true size of the surface projection is somewhat overestimated, even though its rectangular shape is preserved. It should be noted that the selected width ($\theta = 0.5°$) is smaller than the smallest wavelength that can be resolved by the magnetic field synthetic data (i.e., 0.9°).

Figure 5 shows the results we obtained when varying the parameters of the nominal parallelepiped test case. Figures 5a and 5b show the results when varying the thickness. As in Figure 3, they show the histograms of all non-zero dipole moments obtained by the inversion, as a function of longitude (panel a) and latitude (panel b). The remaining panels of Figure 5 show the results when varying the depth to the top (panels c and d), the width $\delta\theta$ (panels e and f) and the magnetization direction (panels g and h). We note that when varying the depth to the top, the parallelepiped's width is slightly adjusted to keep the surface projection the same for all cases, for easier comparison (increasing by up to 0.09°). We observe that the peak of the longitudinal curves is contained within the surface projection of the magnetized bodies. This is in agreement with the fact that the magnetic field data have sufficient spatial resolution to resolve wavelengths equal to the dimension of the parallelepiped along longitude (angular aperture $\phi = 6°$). The peaks of the latitudinal curves are contained within the surface projection of the magnetized bodies with width equal to or greater than $\delta\theta = 1°$ (green, red, and orange curves and shaded areas, respectively). This again is in agreement with what we would expect given the spatial resolution of the magnetic field data. Besides these observations, we notice again that the larger, thicker, or shallower the magnetized body is, the larger the sum of the dipole moments is. As with the case of spherical caps, the cases with vertical magnetization yield the strongest dipole moments, and the horizontal magnetization yields weaker values by a factor of about two, as expected. Moreover, the results are identical for magnetization directions that are directed upwards and downwards.

We then calculated the threshold value that would lead to all retained dipoles falling inside the surface projection of the magnetized body. For the different test cases, we obtained threshold values that vary from 53% to 96% of $m_{\max}$ (see Table 1). The respective success metric, $SM_{\%}$, as defined in Equation 7, varies from 0.33 to 1. Setting the threshold to 30% of $m_{\max}$ improves the results and yields $SM_{30\%}$ values that vary between 0.87 and 0.98. The lowest value of 0.87 is obtained for the largest depth to the top of the magnetized body, which is 40 km. Overall, we find that for the parameters selected here, the surface projection of parallelepipeds can be reconstructed using the fixed threshold of 30% of $m_{\max}$ with SM $\geq$ 0.87.

3.1.3. Magnetized Rectangular Tube

The third shape we considered is that of a tube, where its vertical thickness is locked to 70% of the volume's width, and with the body centered at 45° latitude and 90° longitude. Figure 6, shows the inversion results for the nominal case where the width is 1°, the depth to the top of the magnetized body is 2 km, the length is 6°, and the magnetization direction is vertical ($\alpha = 0°$). We observe that the strongest dipoles describe well the surface projection of the magnetized body and that the dipoles lying outside of the surface projection have at least half the strength (Figure 6c). When we use a threshold such that we retain only dipoles that lie inside the surface projection (orange line in Figure 6d and threshold equal to 50% of $m_{\max}$), the retained dipoles cover fully the surface projection of the magnetized body. When we use the fixed threshold of 30% of $m_{\max}$ (blue line in Figure 6d), the surface projection is fully covered by dipoles, but some dipoles are also retained exterior to the projection and adjacent to its boundary.

Figure 3. Histograms of total dipole moment for the test cases using magnetized spherical caps of varying dimensions. (a) The total dipole moment of all dipoles belonging in a given longitude range, discretized in bins of 1°. (b) The total dipole moment of all dipoles belonging in a given latitude range, discretized in bins of 1°. (c and d) Same as (a and b), but for varying depth to the top of the magnetized body. (e and f) Same as (a and b), but for varying angular aperture $\delta\phi$, where the shaded zones in blue, gray and green represent the surface projection of the spherical caps with angular apertures of 2°, 6°, and 10°, respectively. (g and h) Same as (a and b), but for varying magnetization direction α. Black solid lines in these plots correspond to the nominal case (please note that the y axes vary).

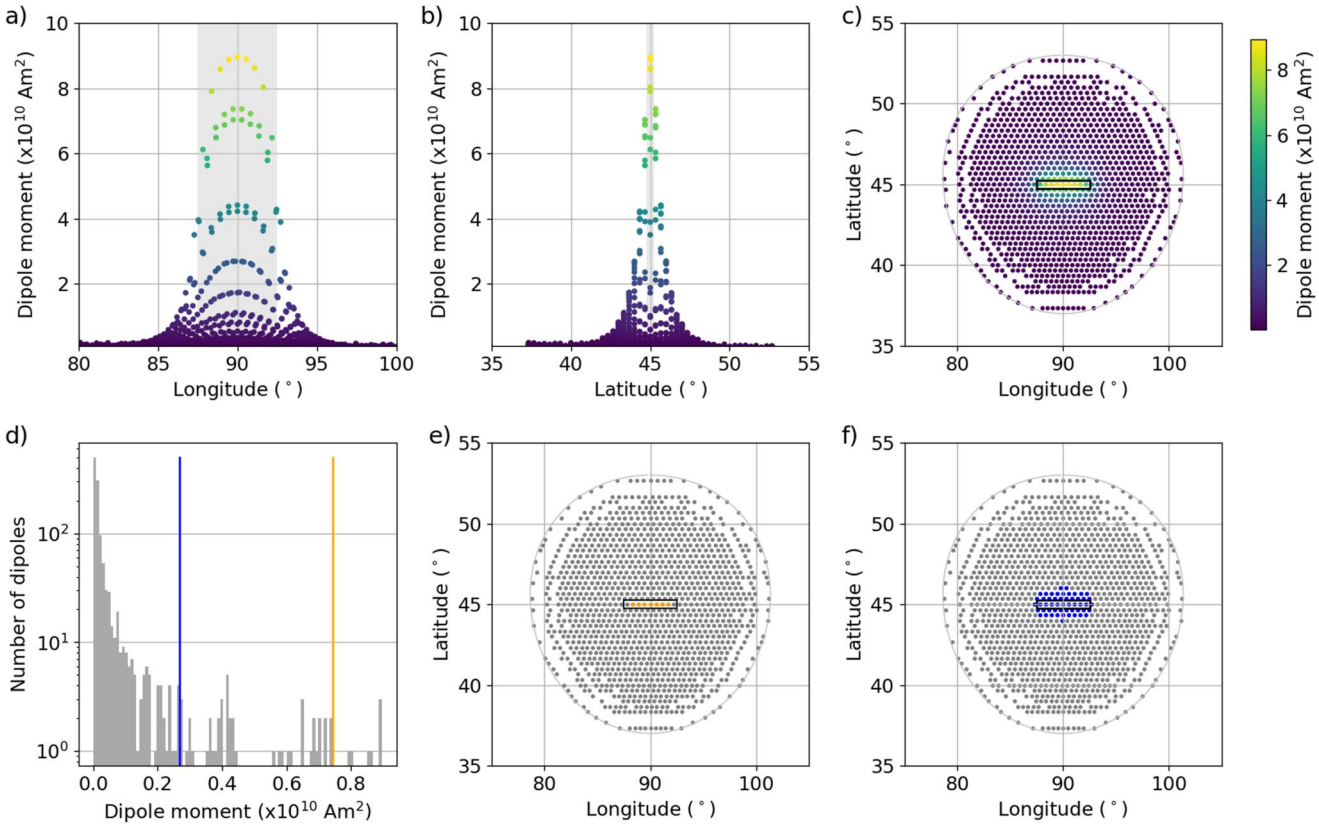

Figure 4. Inversion results of the synthetic magnetized parallelepiped nominal case. All panels are in the same format as Figure 2.

Figure 7 shows histograms of total dipole moment strength when varying the parameters of the nominal case. Figures 7a and 7b show the results when varying the width $\delta\theta$(and corresponding thickness), Figures 7c and 7d show the results when varying the depth to the top, Figures 7e and 7f show the results when varying the length, and Figures 7g and 7h show the results when varying the magnetization direction. We note that when varying the depth to the top, the rectangular tube's width and length are slightly adjusted to keep the surface projection the same for all cases, for easier comparison (increasing by up to 0.01° and 0.2 km, respectively). As for the parallelepiped test cases, we observe that the central part of the longitudinal curve lies within the true surface projection of the magnetized body and this is the case for the longitudinal curves corresponding to magnetized bodies with at least 1° width.

We then calculated the threshold value that would lead to all retained dipoles lying inside the surface projection of the magnetized body. The threshold values we obtained for the various test cases vary from 37% to 72% of $m_{\max}$ (see Table 1). The respective success metric, $SM_{\%}$, as defined in Equation 7, varies from 0.76 to 1, where the lowest value of 0.76 corresponds to the largest depth to the top of the magnetized body we considered, which is 20 km. Setting the threshold to 30% of $m_{\max}$, yields $SM_{30\%}$ values that vary between 0.92 and 0.99, where the lowest value corresponds to the largest width considered here, which is 4°. The second lowest value of 0.94 corresponds to a depth of 20 km to the top of the magnetized body. Overall, for the parameters considered here, we find that the surface projection of rectangular tubes can be reconstructed using the fixed threshold of 30% of $m_{\max}$ with SM > 0.9.

3.2. Realistic Synthetic Cases

To evaluate the performance of Parker's method in retrieving the surface projection of a subsurface three-dimensional magnetized body under realistic conditions, we also performed a series of more realistic synthetic tests that deviate from the idealized cases in the preceding section. In the following subsections, we consider the

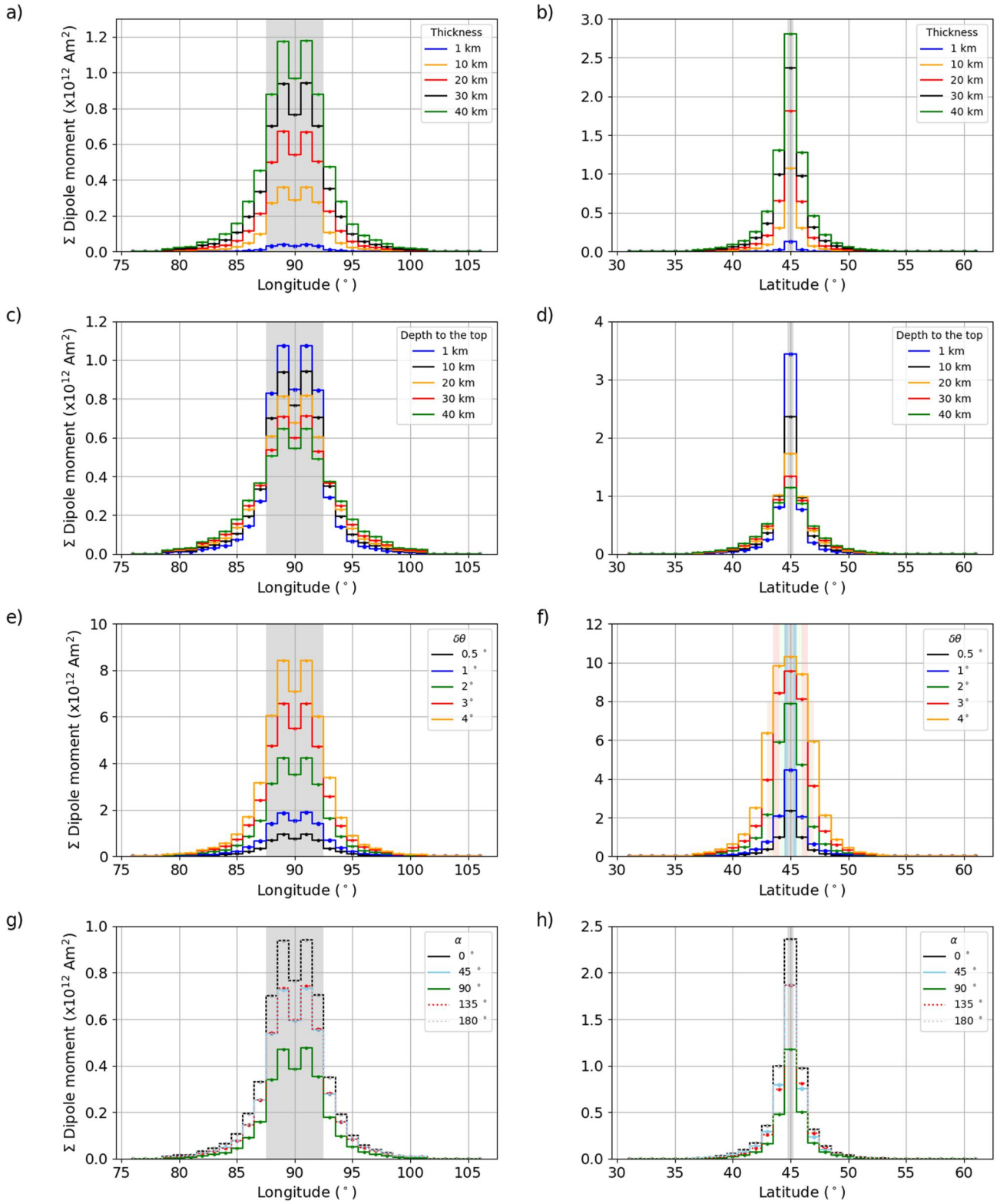

Figure 5. Histograms of total dipole moment for the test cases using magnetized parallelepipeds of varying dimensions. All panels are in the same format as Figure 2.

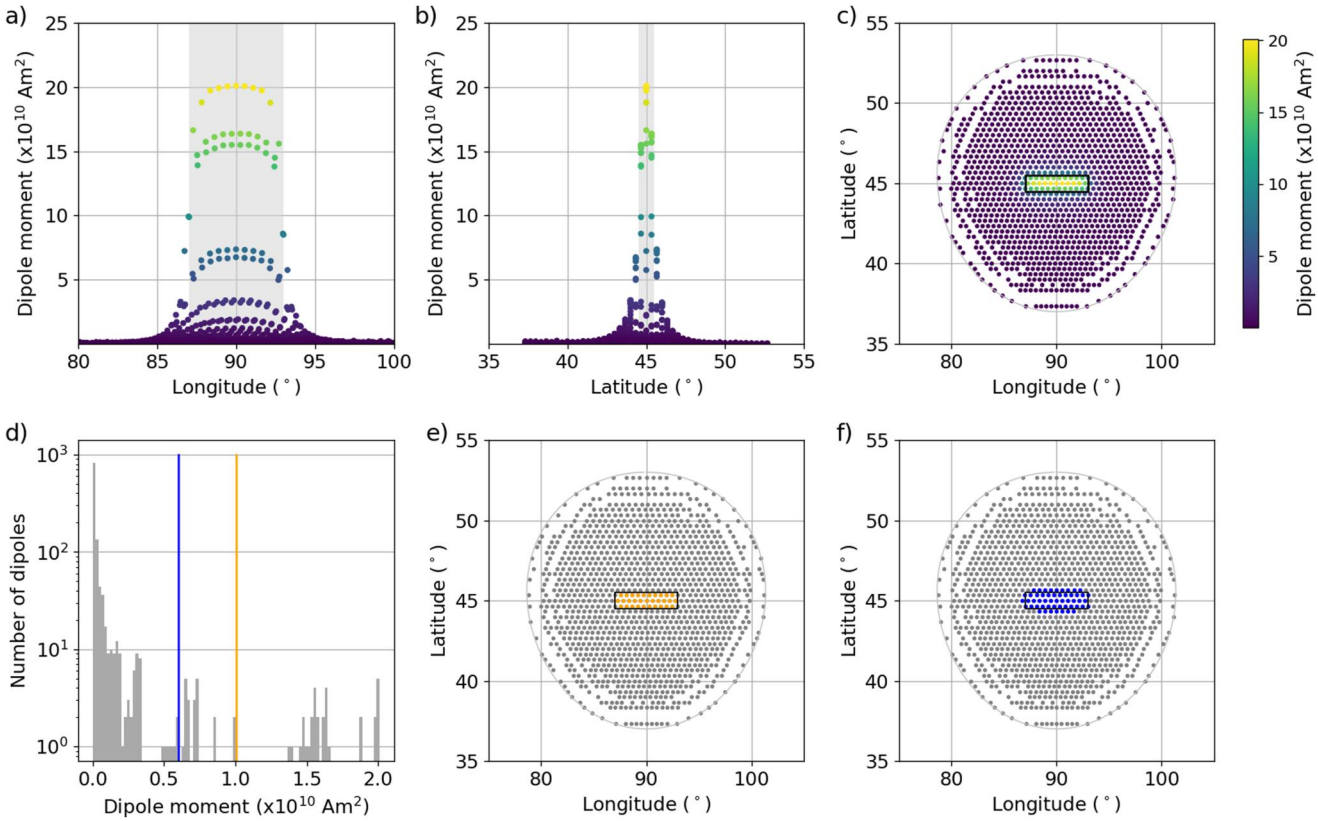

Figure 6. Inversion results of the synthetic rectangular tube nominal case. All panels are in the same format as Figure 2.

effect of measurement noise, lateral variations in the thickness of the magnetized body, and the consequences of non-unidirectional magnetization.

3.2.1. Noisy Magnetic Field Measurements

Noise is intrinsic to any data set. In order to evaluate how noise affects the performance of Parker's method, we repeated the tests of the nominal cases described in Section 3.1 after adding Gaussian noise to the magnetic field observations. When considering the radial component of the synthetic magnetic field at 30 km altitude, we added a zero-mean Gaussian noise, whose standard deviation was 5%, 10% and 20% of the average of the radial magnetic field over the magnetized body. These noise levels are comparable to those found in Tsunakawa et al. (2010). In particular, this corresponds to a standard deviation of 0.5, 1 and 2 nT, respectively, for the spherical cap nominal case, to 0.2, 0.4 and 0.8 nT for the parallelepiped nominal case, and to 0.4, 0.8 and 1.6 nT for the rectangular tube nominal case. Hereafter we refer to these cases as the 5%, 10% and 20% test cases.

Figure 8 shows the distribution of dipole moments we obtained for the spherical cap test cases. Figure 8a shows the histogram of all the non-zero dipole moments obtained from Parker's method for the 5% noise case. As in Section 3.1, the orange line corresponds to the minimum dipole moment of the retained dipoles such that all of them fall within the surface projection of the subsurface body. We find this threshold to be 56% of $m_{\max}$ (see Table 2), and the respective $SM_{\%}$ value is 0.21. Although this threshold only retains about one out of five of the dipoles within the true surface projection, the dipoles are distributed in a way that the circular shape of the projection is recovered. The blue line in Figure 8a corresponds to the threshold of 30% of $m_{\max}$. The retained dipoles when using this threshold are shown in Figure 8c, and the respective $SM_{30\%}$ value is 0.5. Using this threshold, we retain approximately half of the dipoles within the true surface projection. The small number of retained dipoles that are located outside of the projection are found to be adjacent to the projection's boundary, and the circular shape of the surface projection is better recovered. The middle row of this figure plots the same results, but for the 10% noise case. For these tests, the orange line corresponds to 53% of $m_{\max}$, and the respective $SM_{\%}$ value is 0.34. By retaining a few more dipoles than in the 5% test case, the surface projection is recovered

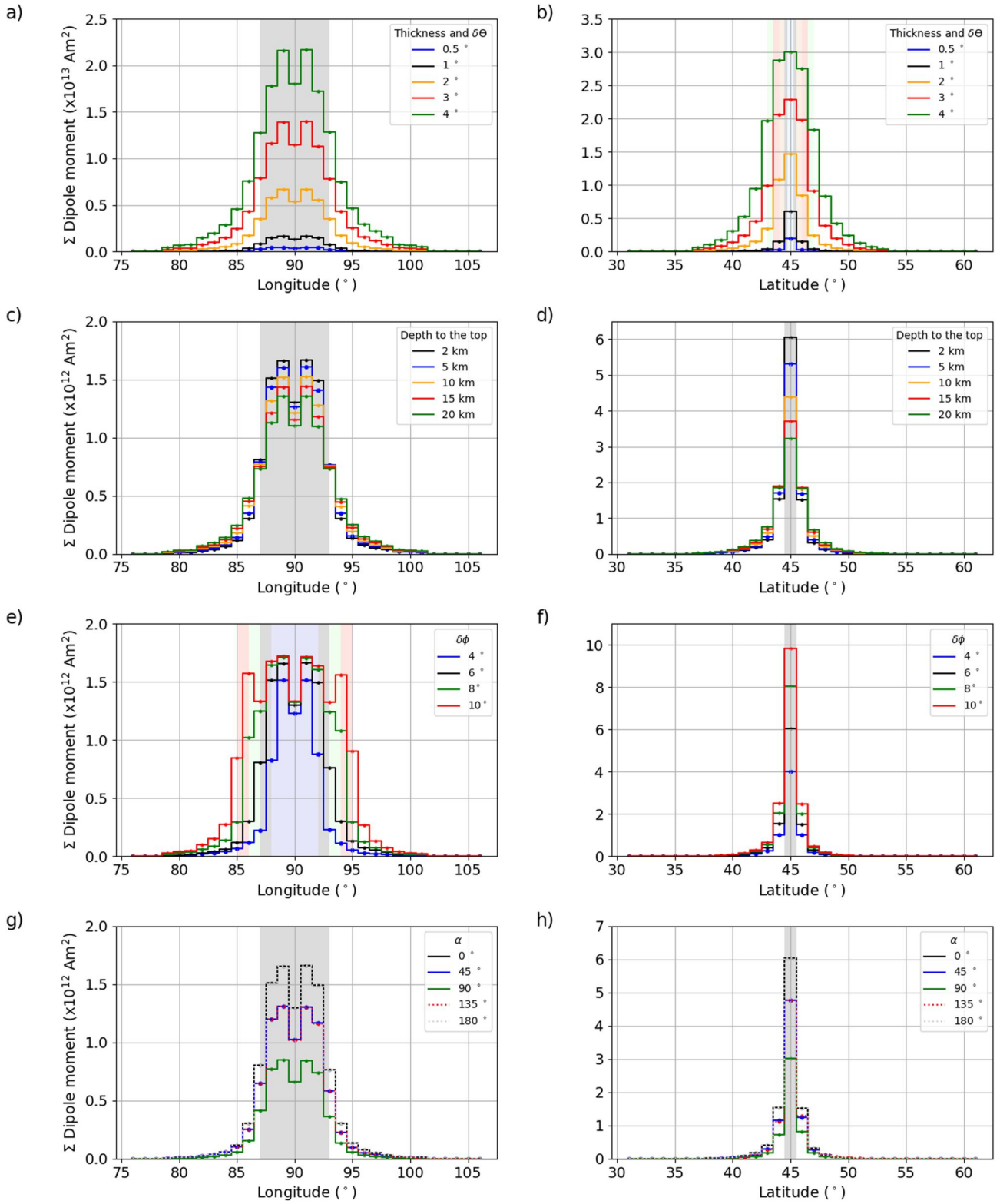

Figure 7. Histograms of total dipole moment for the test cases using magnetized rectangular tubes of varying dimensions. All panels are in the same format as Figure 3.

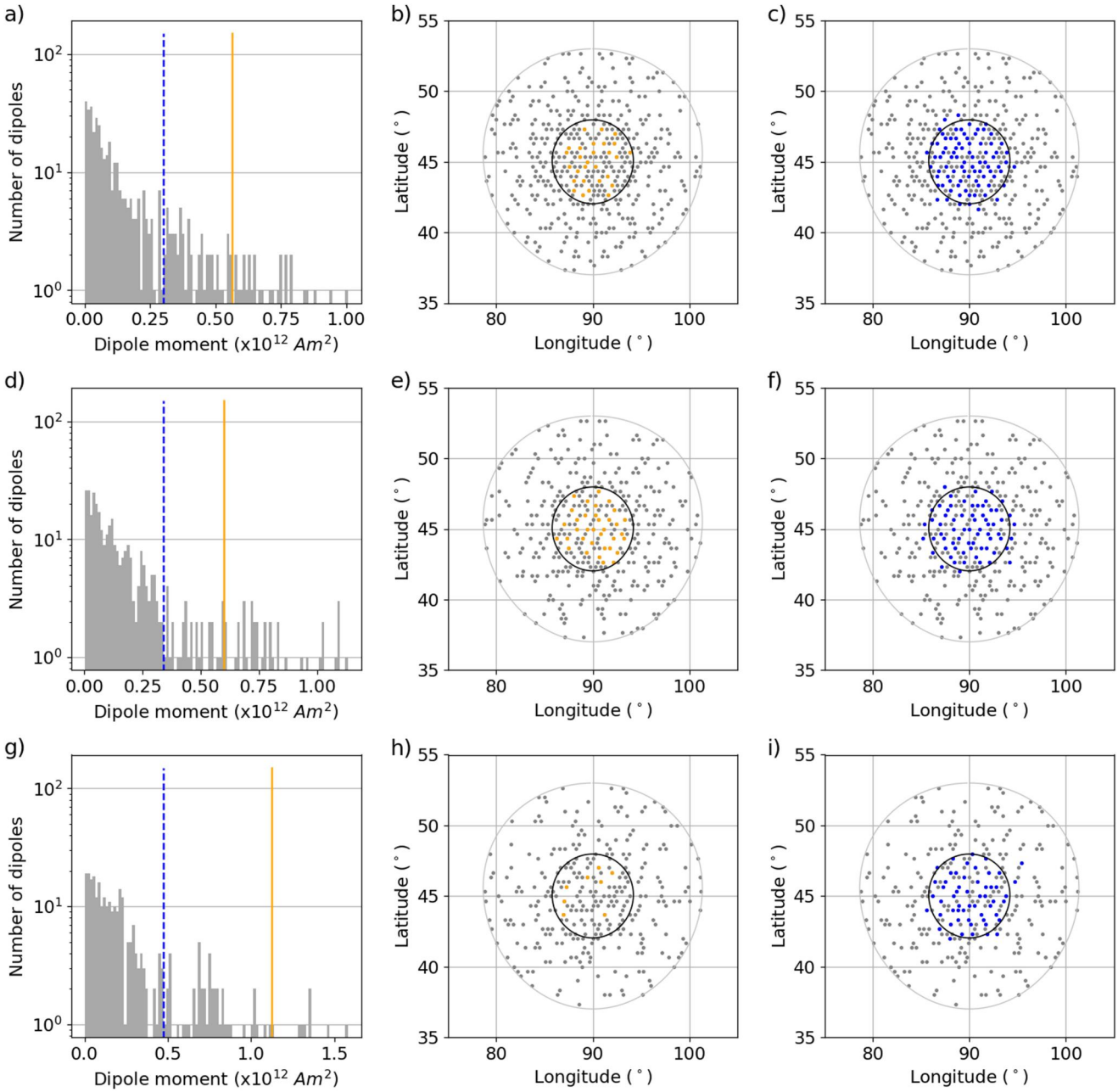

Figure 8. Distribution of dipole moments obtained when adding Gaussian noise to the nominal spherical cap inversion case. (a) The histogram of all non-zero dipole moments obtained using Parker's method when adding 5% measurement noise. The orange line corresponds to the minimum dipole moment such that all dipoles with higher values fall within the surface projection of the subsurface body. The blue line corresponds to 30% of the maximum dipole moment. (b) The location of the retained dipoles when using the value of the orange line for the minimum dipole moment threshold. (c) The location of the retained dipoles when using the value of the blue line for the minimum dipole moment threshold. (d–f) and (g–i) Same as panels (a–c) but for the 10% and 20% noise cases, respectively.

equally well. For the 30% of $m_{\max}$ threshold, marked by the blue line in Figure 8d, we obtain an $SM_{30\%}$ of 0.47, which is only slightly smaller than that of the 5% test case. Finally, the lower row of the figure plots the results for the 20% noise case. For this case, the orange line corresponds to 71% of $m_{\max}$, and the respective $SM_{\%}$ value is 0.21. Contrary to the 5% and 10% cases, the surface projection is not successfully recovered. However, the shape of the projection is successfully retrieved when the threshold is 30% of $m_{\max}$, marked by the blue line in Figure 8g, with an $SM_{30\%}$ of 0.5, which is roughly the same value as for the 5% and 10% test cases. Overall, adding Gaussian

Table 2
Inversion Results When Considering Gaussian Noise Measurement Errors and Lateral Variations in the Bottom Boundary of the Magnetized Bodies

Shape	Bottom	σ_{noise} (nT)	$B_r^{\max}$ (nT)	N	$m_{\min}$ (A m^2)	$m_{\max}$ (A m^2)	Misfit (nT)	Threshold (%)	$SM_{\%}$	$SM_{30\%}$
Spherical cap	Even	0.5	14.06	434	8.5×10^6	1.0×10^{12}	0.44	56	0.21	0.5
	Even	1	15.26	358	5.1×10^8	1.1×10^{12}	0.86	53	0.34	0.47
	Even	2	18.7	297	3.8×10^8	1.58×10^{12}	1.88	71	0.21	0.5
	Uneven	0	8.58	1,032	8.8×10^7	3.6×10^{11}	0.01	49	0.5	0.6
Parallelepiped	Even	0.2	4.60	279	5.5×10^7	2.9×10^{11}	0.16	71	0.2	0.53
	Even	0.4	5.11	245	1.7×10^8	3.3×10^{11}	0.34	79	0	0.33
	Even	0.8	5.4	234	2.7×10^8	3.8×10^{11}	0.67	93	0	0.38
	Uneven	0	3.16	1,034	3.2×10^5	1.3×10^{11}	0.001	73	0.22	0.65
Rectangular tube	Even	0.4	10.01	290	5.2×10^7	4.2×10^{10}	0.39	71	0.21	0.72
	Even	0.8	11.08	249	1.2×10^8	4.5×10^{11}	0.75	80	0.29	0.67
	Even	1.6	12.2	258	3.6×10^8	7.1×10^{11}	1.56	62	0.26	0.66
	Uneven	0	7.80	1,220	5.6×10^5	1.7×10^{11}	0.002	51	0.94	0.99

Note. Each test case uses the nominal geometry from Table 1, and we provide the standard deviation of the measurement noise (σ_{noise}) and the maximum strength of the input radial magnetic field $\left(B_r^{\max}\right)$. The following results from Parker's method are provided in the columns that follow: the number of dipoles with non-zero dipole moment (N), the minimum and maximum dipole moments of the obtained magnetization distribution ($m_{\min}$ and $m_{\max}$, respectively), and the RMS misfit between the radial components of the input and the modeled magnetic field (Misfit). Also shown is the percentage of $m_{\max}$ used as a threshold to define the retained dipoles (Threshold) and the respective success metric ($SM_{\%}$). The last column shows the success metric when using a threshold fixed to 30% of $m_{\max}$ ($SM_{30\%}$).

noise of this intensity to the spherical cap nominal test case does not prohibit the recovery of the surface projection of the magnetized body.

Figure 9 shows analogous results for the nominal parallelepiped test case with Gaussian noise. The dipole moment threshold so that all retained dipoles fall within or on the boundary of the true surface projection is 71% of $m_{\max}$, which corresponds to an $SM_{\%}$ of 0.2. In particular, this threshold retains two out of the five dipoles within the surface projection, which is not sufficient to reconstruct the shape of the body. By using the fixed threshold of 30% of $m_{\max}$, we retain three out of the five dipoles inside the surface projection, but also 17 dipoles that lie outside the projection, within less than 1° distance from its boundary. The respective $SM_{30\%}$ value is 0.53. In this case, while the exact shape of the projection is not well recovered, the location of its center and its elongated shape are well represented. For the 10% noise case, when choosing a threshold such that all retained dipoles lie within the surface projection (79% of $m_{\max}$), no dipole is retained. Using the 30% of $m_{\max}$ threshold, we obtain two dipoles inside the surface projection but most of the retained dipoles lie outside. The outside dipoles lie close to the surface projection but at variable distances, within up to 2° distance from its boundary. This solution allows the approximate localization of the projection's center but provides a distorted view of its shape. Finally, the lower row of the figure plots the results for the 20% noise case. These are similar to the 10% noise case in that no dipole is retained when choosing a threshold such that all retained dipoles lie within the surface projection (93% of $m_{\max}$). But unlike the 10% noise case, the fixed threshold of 30% of $m_{\max}$ does not even allow to localize the center of the surface projection. Most of the selected dipoles lie outside the surface projection and are highly dispersed in a way that does not allow to infer neither the shape of the projection nor its center.

Figure 10 shows the results we obtained for the nominal rectangular tube case with Gaussian noise. For the 5% noise case, the orange line corresponds to 71% of $m_{\max}$, the $SM_{\%}$ value is 0.21, and the $SM_{30\%}$ value is 0.72. Both solutions recover relatively well the shape of the surface projection, with the fixed threshold of 30% performing better. The 10% and 20% noise cases perform similarly to the 5% noise case. Even if the number of the retained dipoles decreases as the noise level increases, the shape and location of the surface projection is recovered. For the 10% noise case, the orange line corresponds to 80% of $m_{\max}$, the value of $SM_{\%}$ is 0.29, and $SM_{30\%}$ is 0.67, while for the 20% noise case, the orange line corresponds to 62% of $m_{\max}$, $SM_{\%}$ is 0.26, and $SM_{30\%}$ is 0.66.

3.2.2. Magnetized Sources With Uneven Bottom

In contrast to the magnetized bodies of the ideal cases considered in Section 3.1, we might expect the bottom of the magnetized sources to be uneven and vary in depth. In order to investigate how this would affect the

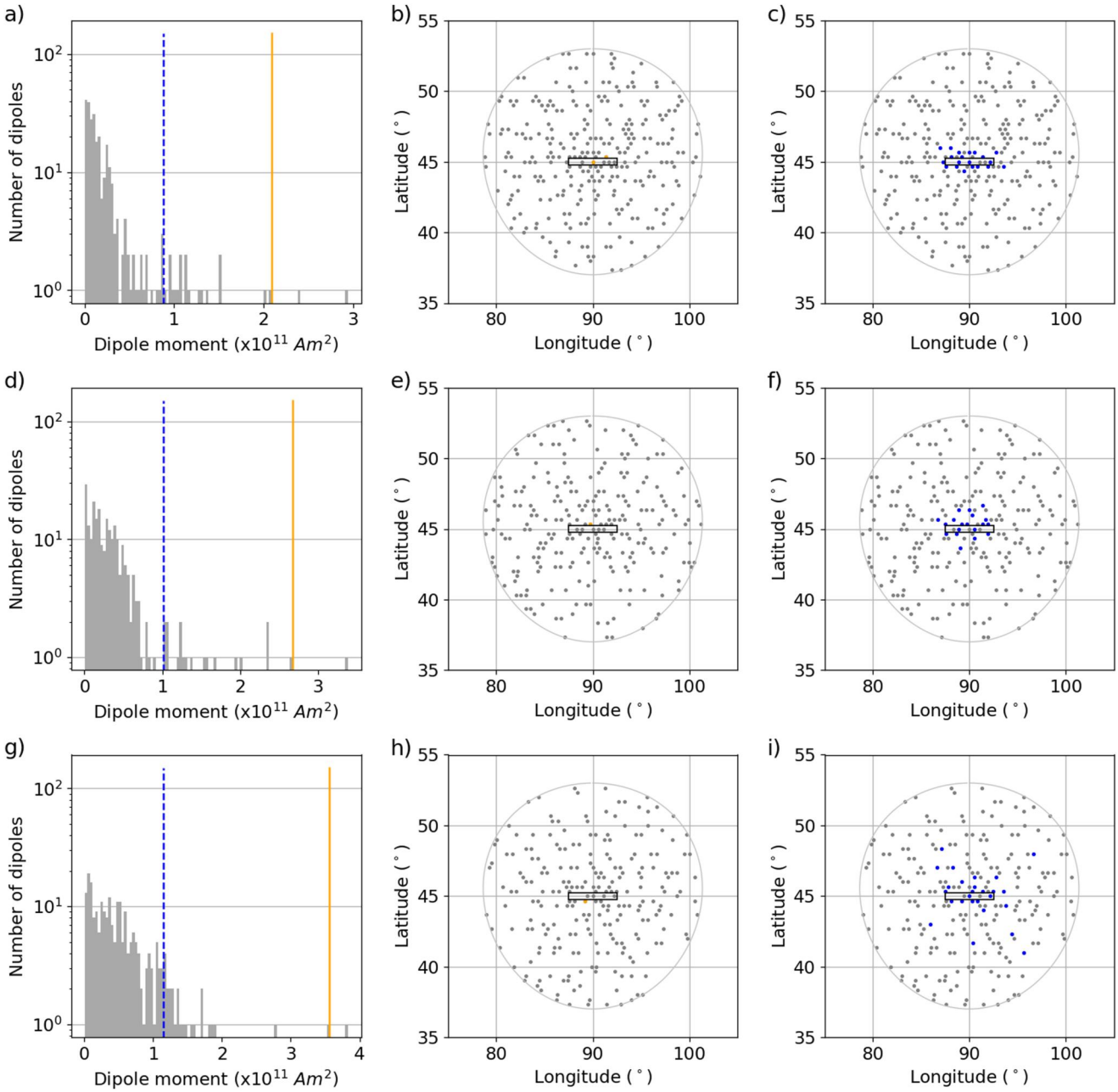

Figure 9. Distribution of dipole moments obtained when adding Gaussian noise to the nominal parallelepiped inversion case. The format of this figure is the same as Figure 8.

estimation of the surface projection of the magnetized body, we add a twist to the nominal cases considered in Section 3.1. Namely, we assign a different thickness to each grid point while keeping the same depth of the uppermost surface of the magnetized body. Each value is a random draw from a uniform distribution, whose values vary between 50% and 100% of the thickness of the nominal case (see values in bold in Table 1). By doing so, we keep intact the surface projection of the magnetized body, while making its bottom surface uneven.

The results are presented in Figure 11. Figures 11a–11c correspond to the spherical cap case, and Figure 11a shows the histogram of all non-zero dipole moments obtained from Parker's method. As with all previous test cases, the orange line corresponds to the minimum dipole moment such that all of the retained dipoles fall within the surface projection of the subsurface body, which is here 49% of m_{max}. The location of the respective dipoles is

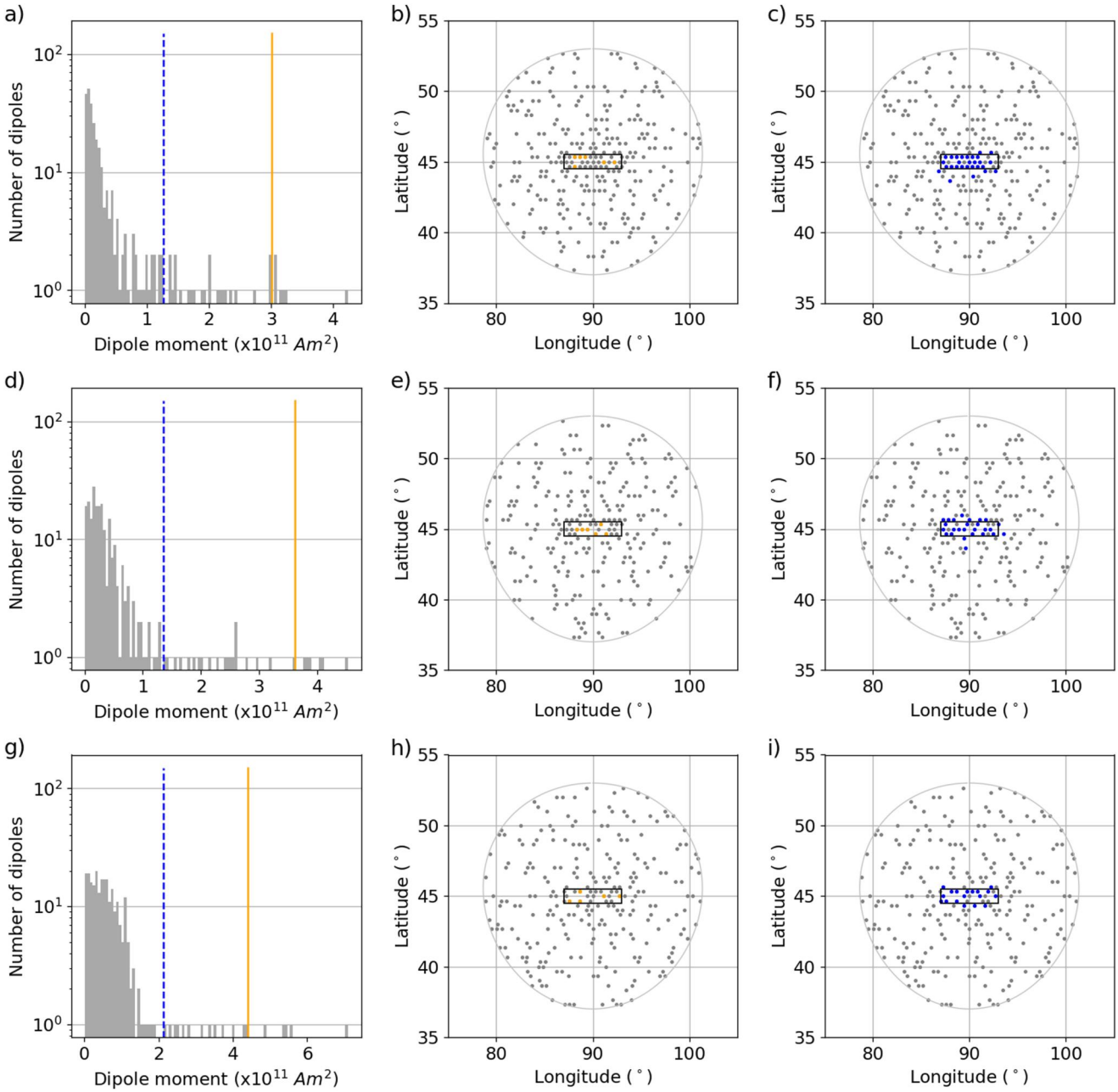

Figure 10. Distribution of dipole moments obtained when adding Gaussian noise to the nominal rectangular tube case. The format of this figure is the same as Figure 8.

shown in Figure 11b and this case corresponds to a success metric $SM_{\%} = 0.5$ (see Table 2). The blue line in Figure 11a corresponds to a dipole moment threshold of 30% of $m_{\max}$. The location of the respective dipoles is shown in Figure 11c and corresponds to $SM_{30\%} = 0.6$. As a comparison, for the case where the thickness is constant, $SM = 0.97$ and $SM_{30\%} = 0.93$. Figures 11d–11f show the results of the parallelepiped test case, for which the orange line corresponds to 73% of the maximum dipole moment. For this test case, we find $SM_{\%} = 0.22$ and $SM_{30\%} = 0.65$, in contrast to $SM_{\%} = 0.78$ and $SM_{30\%} = 0.96$, for the case where the thickness is constant. Figures 11g and 11h show the results of the rectangular tube case, for which the orange line corresponds to 51% of $m_{\max}$. For this test case, $SM_{\%} = 0.94$ and $SM_{30\%} = 0.99$, which is almost identical to the respective case with constant thickness, for which $SM_{\%} = 0.94$ and $SM_{30\%} = 0.98$.

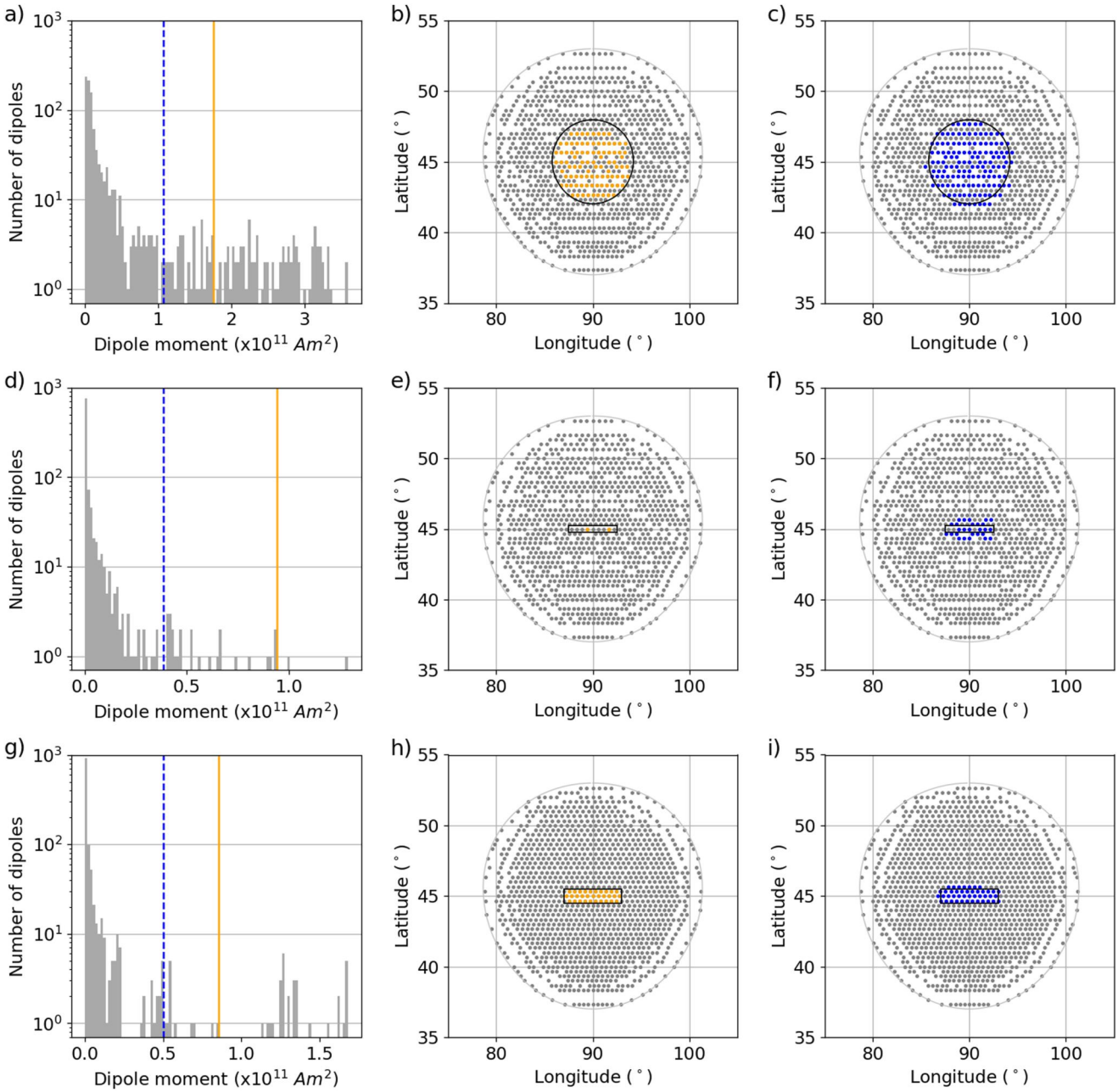

Figure 11. Distribution of dipole moments obtained when considering a variable depth of the bottom surface of the magnetized bodies. (a) Histogram of the dipole moment strength when considering a spherical cap. (b) The location of the dipoles whose dipole moment strength is stronger than the value depicted by the orange line in panel (a). (c) The location of the dipoles whose dipole moment strength is stronger than the value depicted by the blue line in panel (a). (d–f) Same as panels (a–c), when considering a parallelepiped. (g–i) Same as panels (a–c), when considering a rectangular tube.

The rectangular tubes cases give the best results. Both thresholds perfectly recover the surface projection of the magnetized body, which is evident from the $SM_{\%}$ and $SM_{30\%}$ metrics being close to 1. The surface projection of the magnetized spherical cap is also very well recovered. While not all dipoles inside the true surface projection are retained, the distribution of the retained dipoles is such that the shape of the body can be accurately reconstructed, especially when using the fixed 30% threshold. The cases that give the least satisfactory results is that of the magnetized parallelepipeds. But even in this case, the rough outline of the surface projection of the body is recovered, although its width is overestimated.

Table 3
Inversion Results for the Case of Two Spherical Caps With Different Magnetization Directions

Scenario	$\delta\alpha$ (°)	$B_r^{\max}$ (nT)	N	$m_{\min}$ (A m^2)	$m_{\max}$ (A m^2)	Misfit (nT)	Threshold (%)	$SM_{\%}$	$SM_{30\%}$
Attached	0	12.77	1,198	4.96×10^7	2.55×10^{11}	0.04	71	0.59	0.9
	45	12.89	1,160	2.68×10^7	2.55×10^{11}	0.04	67	0.62	0.9
	90	13.20	933	2.05×10^7	2.83×10^{11}	0.12	78	0.44	0.78
	135	13.56	642	2.08×10^7	4.48×10^{11}	0.5	84	0.07	0.63
	180	13.7	528	4.36×10^8	5.34×10^{11}	0.69	93	0.04	0.55
Superposed	0	18.01	1,189	2.53×10^6	3.56×10^{11}	0.04	46	0.88	0.99
	45	16.21	1,205	1.43×10^8	3.24×10^{11}	0.04	51	0.78	0.94
	90	13.54	1,043	5.69×10^7	2.88×10^{11}	0.06	54	0.75	0.85
	135	13.66	723	1.00×10^8	4.59×10^{11}	0.33	55	0.47	0.77
	180	13.76	616	6.15×10^7	6.72×10^{11}	0.5	53	0.25	0.64

Note. For each test case, we show the angular separation between the magnetization directions of the two spherical caps ($\delta\alpha$), the maximum strength of the input radial magnetic field $\left(B_r^{\max}\right)$, and the following results from Parker's method: the number of dipoles with non-zero dipole moment (N), the minimum and maximum dipole moments of the obtained magnetization distribution ($m_{\min}$ and $m_{\max}$, respectively), and the RMS misfit between the radial components of the input and the modeled magnetic field (Misfit). Also shown is the percentage of $m_{\max}$ used as a threshold to define the retained dipoles (Threshold) and the respective success metric ($SM_{\%}$). The last column shows the success metric when using a threshold fixed to 30% of $m_{\max}$ ($SM_{30\%}$).

3.2.3. Non-Unidirectional Magnetized Sources

Next we evaluate the performance of Parker's method when the assumption of unidirectional magnetization, the key assumption of this method, is clearly violated. As already mentioned in Section 2.2, no magnetization distribution generated by an internal dipole of a planetary body is strictly unidirectional. However, the smaller the size of the source, the closer to unidirectional will be the magnetizing field. In this section, we go a step further than simply assuming large bodies and consider two magnetized spherical caps, each with different lateral sizes, thicknesses and magnetization directions. We center the first spherical cap at longitude 90° and latitude 45°, and assign to it an angular aperture of 6°, a thickness of 20 km, and radial magnetization (i.e., $\alpha_1 = 0°$). We assign to the second spherical cap an angular aperture of 4°, a thickness of 13 km, and we let its magnetization direction vary from parallel to anti-parallel with respect to the magnetization of the first spherical cap, in increments of 45°. As for the location of the second spherical cap, we consider two different scenarios: (a) the two spherical caps are attached to each other on the side and (b) the two spherical caps are partially superposed, such that over the region that their surfaces overlap, the magnetization is the vector sum of the magnetization of the two spherical caps. The results using both a tailored and a fixed threshold are presented in Table 3. Figures 12 and 13 show the results when using the fixed threshold of 30%.

Figures 12a and 12b show histograms of total dipole moment as a function of longitude and latitude for the cases of attached spherical caps. We observe that when the angular separation between the two magnetization directions, $\delta\alpha$, is zero, the longitudinal curve is asymmetric, with its peak located at the center of the largest spherical cap and the tale on the side of the secondary cap covering that cap's surface projection. As $\delta\alpha$ increases, the longitudinal curve becomes more and more symmetric and its peak is shifted away from the center of the first cap, toward the center of the second one, while it also gains in amplitude. The latitudinal curves are symmetric about the center of both spherical caps at 45°. Figures 12c and 12d show the respective curves obtained for the test cases of the superposed spherical caps. Here, the longitudinal curve starts out as a symmetric curve and becomes more asymmetric as $\delta\alpha$ increases.

Figure 13 shows the location of the retained dipoles (gray points), as well as those with moments that are greater than 30% of $m_{\max}$ (orange points). We observe that when $\delta\alpha$ is up to 45°, the surface projection of both bodies is recovered with high accuracy ($SM_{30\%}$ at least 90%). As $\delta\alpha$ increases, the projection of the smaller body starts to be less accurate until it is not discernible ($\delta\alpha \geq 135°$). The surface projection of the larger body remains fairly well recovered even for $\delta\alpha = 180°$.

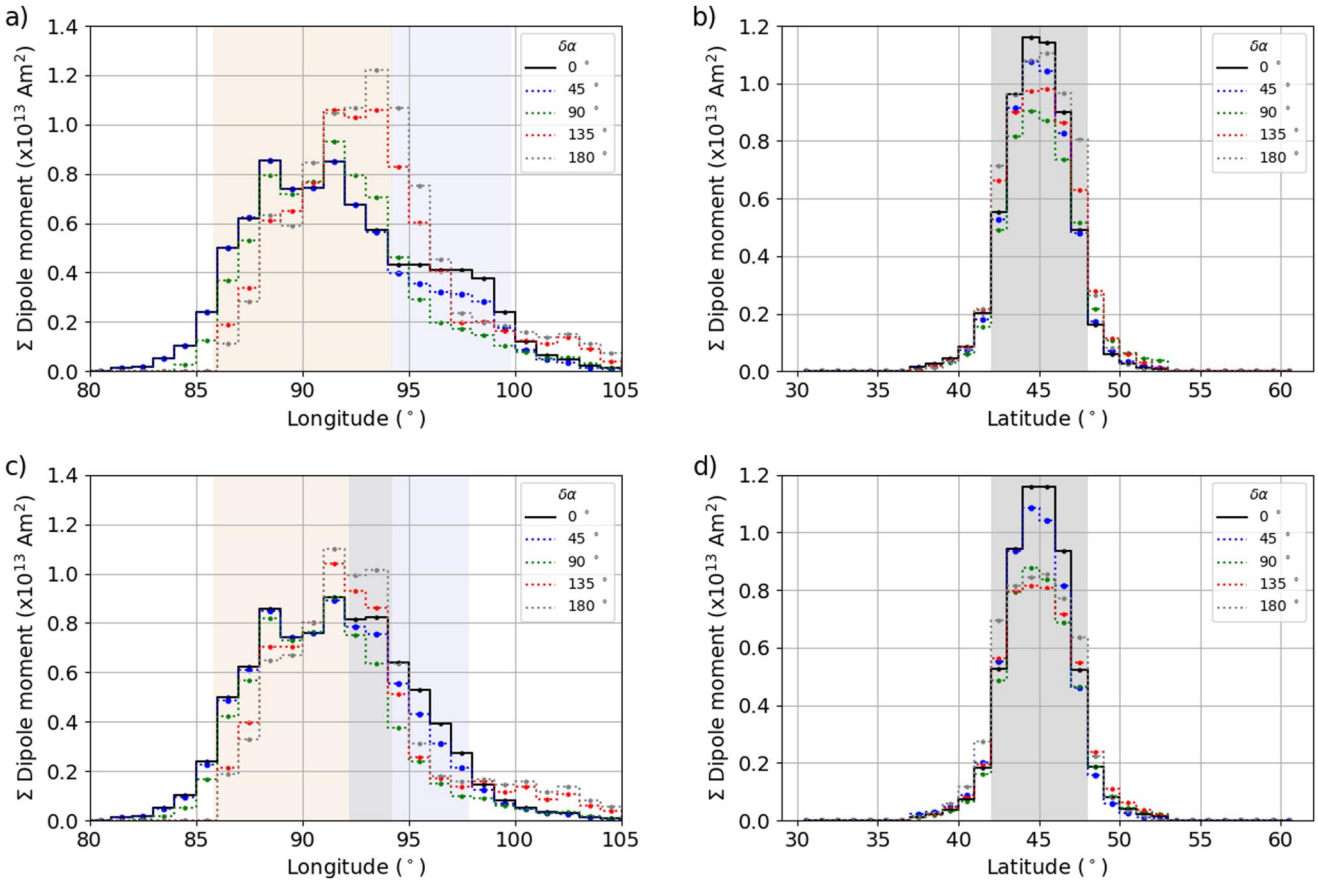

Figure 12. Histograms of total dipole moment for the test cases with two spherical caps. The histograms are shown as a function of longitude (a and c) and latitude (b and d). The upper row (a and b) shows the results when the two spherical caps are attached and the lower row (c and d) show the results when the two caps are partially superposed. Orange and blue shaded zones represent the surface projection of the two spherical caps, while the gray shaded zone represents the area where they overlap. The difference in the direction of magnetization of the two spherical caps, $\delta\alpha$ is provided in the legend for each plot.

4. Application to Two Lunar Magnetic Anomalies

As a final evaluation of the ability of Parker's method to reconstruct the surface projection of a real-world subsurface magnetized body, we apply it to two lunar magnetic anomalies that correspond to prominent and previously studied geological features: the magnetic anomaly within the Mendel-Rydberg impact basin and the magnetic anomaly associated with the Reiner Gamma swirl albedo marking. The results are presented in Figure 14.

As input to these two inversions, we use the lunar magnetic field maps of Tsunakawa et al. (2015), which are based on Lunar Prospector and Kaguya vector magnetic field measurements. In particular, we use their maps of the radial magnetic field component at 30 km altitude, with a 0.5° spacing. An equidistant grid with a 0.4° spacing at the equator (Katanforoush & Shahshahani, 2003) for the surface dipoles was then centered over and encompassing the magnetic anomaly.

4.1. Mendel-Rydberg Impact Basin

The Mendel-Rydberg magnetic anomaly is correlated with the Mendel-Rydberg multi-ring impact basin that is characterized by a main basin rim, a probable peak ring and an inner depression, whose diameters are 650 km, 325 and 203 km, respectively (Neumann et al., 2015). All three rings are highlighted as black circles in the left panels of Figure 14. Topography and the related magnetic anomaly, are shown in Figures 14a and 14c. The strongest signals are observed within the southwest portion of the inner depression. The main magnetic anomaly consists of two peaks with different magnetic intensities and the maximum magnetic field strength at 30 km altitude is about

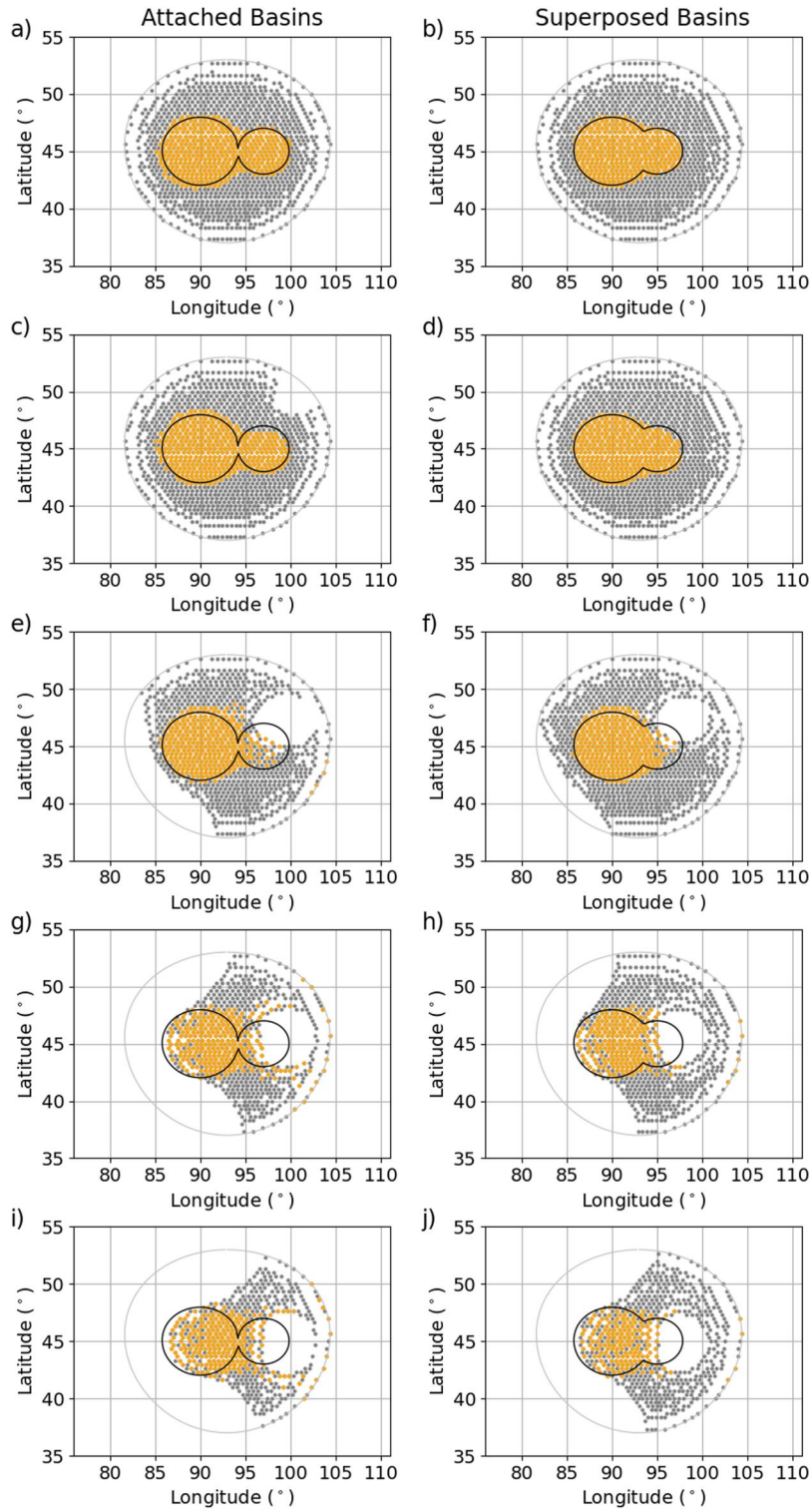

Figure 13. Locations of the non-zero dipoles for the test cases with two spherical caps with different magnetization directions. The left column shows the case where the two spherical caps are attached, whereas the right column shows the case where the two caps are partially superposed. The angular deviation between their magnetizations is (a and b) 0°, (c and d) 45°, (e and f) 90°, (g and h) 135°, and (i and j) 180°. The black line delimits the boundary of the two spherical caps and the silver line delimits the boundary of the grid of dipoles. The orange points correspond to those dipoles whose magnetic moment is more than 30% of $m_{\max}$.

10.1029/2023JE008125

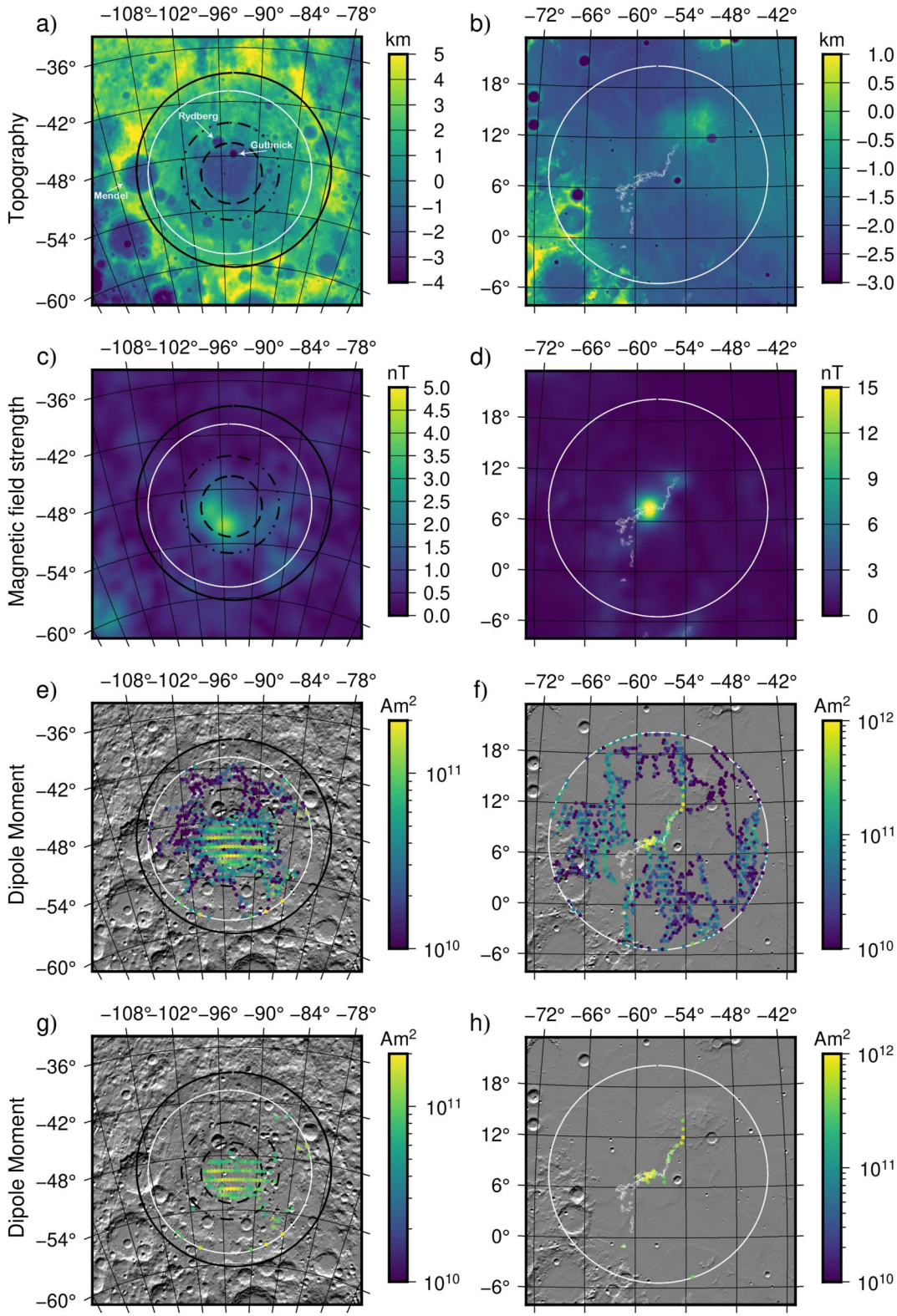

Figure 14.

5 nT. Considerably weaker magnetic field signals are found between the main rim and the inner depression (eastern and southeastern region), with the strongest being about 2 nT.

Oliveira et al. (2017) previously used Parker's method to infer the distribution of magnetization within this basin and proposed that the origin of the magnetic anomaly could be the result of iron-rich projectile materials delivered to the lunar surface and incorporated into the impact melt sheet during the impact. For their inversion, they selected the magnetic field data within a grid of 10° angular radius, which encompasses most of the basin. The inversion solution with the lowest RMS misfit (0.21 nT) provided the dipoles, whose positions and strengths are shown in Figure 14e. The solution comprises 588 dipole with non-zero dipole moments, with strengths ranging from 8.5×10^7 to 3.6×10^{11} A m^2 (see Figure S1 in Supporting Information S1).

Here, rather than considering all dipoles as part of the solution, we use the 30% of m_{max} threshold established from our synthetic tests in order to constrain the surface projection of the 3D magnetization distribution. The position and strength of the retained dipoles are shown in Figure 14g. We see that the vast majority of the retained dipoles fall within the basin's inner depression, which is nearly entirely covered. Only in its most northmost part, northward of 48° South, is there an absence of retained dipoles. This lack of retained dipoles is perhaps correlated with the young superposed Rydberg and Guthnick craters, which have diameters of 49 and 36 km, respectively. When using the 30% of m_{max} criteria, only 32 out of 112 of the retained dipoles are located outside of the inner depression. If it were known a priori that all magnetization was located within the inner depression, this would correspond to a success metric SM of 36%. When using these retained dipoles, we find that 72% of the total dipole moment is located within the inner depression. The dipoles exterior to inner depression are mostly found in the southeast half of the basin, where they have a somewhat random distribution. In contrast, there are almost no retained dipoles in the northwest half of the basin exterior to the inner depression.

This retained dipoles distribution using the 30% of m_{max} criteria is similar to the distributions we obtained from the spherical cap synthetic test cases described in Section 3. This suggests that the Mendel-Rydberg magnetic anomaly is the result of a magnetized disk whose magnetization is approximately unidirectional, and whose thickness is not too variable. This result offers evidence in favor of the scenario where the magnetization is a result of the impact basin's central impact melt pool, which is expected to correspond to the central depression (e.g., Vaughan et al., 2013). The enhanced magnetization with respect to the surroundings is plausibly a result of the incorporation of small amounts of iron-rich impactor materials into the impact melt sheet (Oliveira et al., 2017; Wieczorek et al., 2012), which acquired a thermoremanent magnetization as the impact melt sheet cooled. The lack of magnetization in the northernmost portion of the central depression could be a result of two young superposed impact craters in this region (Rydberg and Guthnick) that could have demagnetized the crust by the passage of their shock wave, or by having excavated pre-existing magnetized materials. The few strongly magnetized dipoles retained outside the inner depression could correspond to small pockets of impact melt that were entrained in the excavation flow field (e.g., Galluzzi et al., 2021). The maximum magnetization within the basin is located in the south-west portion of the inner depression, perhaps suggesting a bolide trajectory from the northeast to southwest (e.g., Hood, Oliveira, et al., 2021). However, the slight enhancement of magnetization exterior to the inner depression in the south-eastern half of the basin could alternatively suggest a trajectory from the northwest to the southeast.

4.2. Reiner Gamma

The Reiner Gamma magnetic anomaly is located in a region of flat terrain of basaltic origin, southwest of the Marius Hills volcanic complex (Garrick-Bethell & Kelley, 2019; Hemingway & Garrick-Bethell, 2012; Hemingway & Tikoo, 2018; Hood & Schubert, 1980). Notably, it is correlated with a strong albedo anomaly that is either the result variable rates of space weathering caused by interactions of the solar wind with the magnetic

Figure 14. Distribution and strength of surface dipoles using Parker's method over two lunar magnetic anomalies: the Mendel-Rydberg impact basin (left) and the Reiner Gamma albedo marking (right). Topographic maps are shown in the upper row (a and b), the observed magnetic field strength at 30 km altitude is shown in the second row (c and d), and the location and strength of all dipoles with non-zero magnetic moments are shown in the third row superposed on a shaded relief map derived from the surface topography (e and f). The last row (g and h) shows only those dipoles whose strength is more than 30% of m_{max}. White circles delimit the regions where a priori dipoles were distributed on the surface, black circles delimit the basin main rim (solid line), peak ring (dash-dotted line), and inner depression (dashed line), using the diameters of Neumann et al. (2015). White dots in the right panel delimit the Reiner Gamma albedo anomalies (Denevi et al., 2016). All maps are shown in a Lambert azimuthal equal area projection.

anomaly (e.g., Bamford et al., 2016; Hood & Williams, 1989), or the result of electrostatic sorting of fine surface materials (Garrick-Bethell et al., 2011). This magnetic anomaly, which is one of the strongest on the Moon, is currently the target for the planned Lunar Vertex mission (Blewett et al., 2022).

The Reiner Gamma swirl can be divided into three parts: (a) the main body, distributed over longitudes ranging between 58 and 60°W and latitudes ranging between 6 and 8°N; (b) the tail, northeast of the main body, which coincides with an elongated albedo anomaly; and (c) a cluster of mini swirls located southwest of the main body. The swirl's main body corresponds to a magnetic anomaly of about 20 nT at 30 km altitude, whereas the swirl's tail corresponds to a weaker magnetic field anomaly of 7 nT (Tsunakawa et al., 2015). The cluster of mini swirls is only associated with weak magnetic field signals. The origin of this magnetic anomaly is still under debate. Suggested scenarios include a thin near-surface layer of impact ejecta (Hood et al., 2001; Hood, Torres, et al., 2021; Nicholas et al., 2007), an intrusive magmatic dike (Hemingway & Tikoo, 2018), and a buried crater that was later filled by volcanic material (Kelley & Garrick-Bethell, 2020).

For our inversion, we placed the dipoles on the surface within a circle with an angular radius of 13° and we considered magnetic field data within a larger circle with an angular radius of 14°. These circle sizes encompass the entirety of the magnetic anomaly and the adjacent Marius Hills volcanic complex. This anomaly was previously studied by Oliveira and Wieczorek (2017) for paleopole location purposes, but they investigated a much smaller study area than here that did not include all of Marius Hills. Our best fitting solution gives an RMS misfit of 0.4 nT, and the position and strength of all non-zero dipoles are shown in Figure 14f. The dipole moments range from about 10^6 to 10^{12} A m^2, spanning six orders of magnitude (see Figure S1 in Supporting Information S1), with the strongest dipoles being coincident with the main Reiner Gamma body and tail. In Figure 14h, we plot only those dipoles whose magnetic moments are at least 30% of m_{max}. We observe that almost all the retained dipoles coincide with the swirl's main body and tail, and that a few extend northward from the end of the tail to the center of the Marius Hills volcanic complex. No dipoles from Parker's inversion are located in the cluster of mini-swirls to the southwest of the main body.

This distribution of dipoles in our inversion is similar to the results we obtained from the parallelepiped synthetic test cases. This suggests that the magnetism responsible for the Reiner Gamma anomaly is thin and elongated. Given that much of the anomaly is represented by a string of dipoles, the width of the magnetized region should be comparable to our dipole grid spacing, which is about 12 km. Portions of the main body are represented by several dipoles tangential to the main strike of the body, suggesting that the width of the magnetized region could extend up to 45 km in places. The shape of the magnetized region that we infer is consistent with a thin magmatic dike, or a swarm of even thinner dikes, as previously inferred by Hemingway and Tikoo (2018). Given that the magnetization in the tail extends into the heart of Marius Hills, the most plausible interpretation is that the dike emanated from this region, propagated downhill to the southwest, and that the magma then accumulated near the main albedo body. The magma near the main body could have either accumulated in the form of an intrusive body, or could perhaps have erupted at the surface (being resurfaced at a later date). The reason that only one such dike emanating from Marius Hills is magnetized remains enigmatic. This could perhaps be a reflection of its age and the temporal variability of the lunar dynamo, or it could perhaps be related to the magma having an atypical iron-metal rich composition. Further progress on deciphering the origin of this anomaly will become possible thanks to the magnetic field measurements collected by the Lunar Vertex mission. In particular, the rover of this mission will obtain magnetic field measurements at the lunar surface, while the lander will obtain measurements along the descent trajectory (Blewett et al., 2022). Parker's method can be applied on data sets obtained at different altitudes. Therefore, these data can be included in the inversion scheme of Parker's method, along with the spacecraft data, to better constrain the inversion, or they can be used in tandem with results from Parker's method to disentangle the sources' depth and magnetization strength.

5. Conclusions

In this study, we evaluated the performance of the inversion technique known as Parker's method (Parker, 1991) in constraining the location and geometry of subsurface magnetic sources. This technique relies on the assumption that the underlying magnetic source of a given anomaly is unidirectionally magnetized, but otherwise makes no other assumptions about the geometry of the source. Given a set of magnetic field measurements, the solution consists of a set of dipoles distributed over the surface that best fits the magnetic field data. This inversion technique was developed initially to determine the best fitting direction of crustal magnetization for a given

magnetic anomaly, and here we tested how faithfully the surface dipoles matched the two-dimension projection of the underlying three-dimensional magnetization.

We performed a series of synthetic tests using known bodies magnetized by an internal dipolar magnetic field and compared the solution of the inversion with the known surface projection of the underlying magnetized body. Aiming to study various geological structures that could be the source of lunar magnetic anomalies, we considered magnetized bodies with spherical cap or parallelepiped shapes, and for each magnetized body, we ran a series of synthetic tests by varying the thickness, depth to the top layer, lateral size and magnetization direction. We also investigated the effect of Gaussian noise in the magnetic field measurements, the effect of magnetized bodies with variable thicknesses, and the effect of non-unidirectionally magnetization. Our results show that by considering as part of the solution only those dipoles whose dipole moment is at least 30% of the maximum dipole moment, the method can delineate the two-dimensional surface projection of a subsurface three-dimensional magnetization distribution as long as the available data have sufficient spatial resolution with respect to the dimensions of the surface projection. We found that if it's not the case, the method still recovers the overall shape and simply overestimates its dimensions. The addition of noise in certain cases did not allow for the accurate reconstruction of the shape of the surface projection but allowed for the localization of its center. The only test case that failed was when the dimensions of the body were smaller than the spatial resolution of the data and in addition the data were quite noisy (20% noise case on the nominal parallelepiped test case). The recovery of the distribution of magnetization was found to be acceptable even when the direction of magnetization varied by up to 45°.

As an application of this technique, we applied Parker's method on two lunar magnetic anomalies. The origin of most lunar magnetic anomalies remains largely unknown. Here, we focused on two anomalies that are associated with prominent geological features. In particular, we focused on, the anomaly that is associated with the Mendel-Rydberg impact basin, and on the anomaly that is associated with the Reiner Gamma albedo marking. Our results show that for the Mendel-Rydberg impact basin, the strongest dipoles obtained by the inversion correlate well with the inner depression of the basin. The inner depression likely corresponds to the thick impact melt sheet of the basin, and the strong magnetizations are plausibly a result of the incorporation of iron-rich impactor materials into the melt sheet. For the Reiner Gamma anomaly, we find that magnetization likely corresponds to a dike that emanates from the center of the Marius Hills volcanic complex. The width of this dike (or dike swarm) is in most places comparable to the resolution of our grid (about 10 km), but it could be up to 45 km wide in the main body of the anomaly.

Future applications of this method will help in delineating the subsurface magnetic anomalies, not only on the Moon, but also on any other terrestrial planetary body for which magnetic field measurements at various altitudes (e.g., through spacecrafts, helicopters, landers or rovers) are or will become available, such as planets Mercury, Earth, Mars and asteroid Psyche. This in turn can help constrain the geological history and surface processes of these bodies, particularly when combined with prior geological information.

Appendix A: The Relationship Between a 3D Magnetization Distribution and the Generated Magnetic Field

The magnetic potential V at point $\mathbf{r} = (r,\theta,\phi)$ due to a magnetization distribution $\mathbf{M}$ that lies in the volume Ω' writes (e.g., Blakely, 1996, Equation 5.2)

$$V(\mathbf{r}) = \frac{\mu_0}{4\pi}\int_{\Omega'} \mathbf{M}(\mathbf{r}')\nabla' \frac{1}{|\mathbf{r}-\mathbf{r}'|} d\Omega', \tag{A1}$$

where $d\Omega' = r'^2 \sin\theta' d\theta' d\phi' dr'$.

Expanding the term $\frac{1}{|\mathbf{r}-\mathbf{r}'|}$ in Spherical Harmonics (e.g., Gubbins et al., 2011, Equation B7), gives

$$\frac{1}{|\mathbf{r}-\mathbf{r}'|} = \frac{1}{r}\sum_{l=0}^{\infty}\sum_{m=-l}^{l}\left(\frac{r'}{r}\right)^l Y_l^m(\theta,\phi)\, Y_l^m(\theta',\phi'), \tag{A2}$$

where $Y_l^m(\theta,\phi)$ are the Schmidt semi-normalized real Spherical Harmonics of degree l and order m, whose expression is

$$Y_l^m(\theta,\phi)=\begin{cases}P_l^m(\cos\theta)\cos(m\phi), & \forall\, m\geq 0\\ P_l^m(\cos\theta)\sin(m\phi), & \forall\, m<0\end{cases} \tag{A3}$$

and whose norm is given by $\int_S Y_l^m Y_{l'}^{m'} dS=\frac{4\pi}{2l+1}\delta_{ll'}\delta_{mm'}$.

Introducing Equation A2 into Equation A1, we obtain

$$\begin{aligned}V(\mathbf{r})=\frac{\mu_0}{4\pi}\sum_l\sum_m Y_l^m(\theta,\phi)\Bigg\{&l\int_{r'=r_1}^{r'=r_2}\int_{\theta',\phi'}\mathbf{M}_r(\theta',\phi')\left[\frac{r'(\theta',\phi')}{r}\right]^{l+1}Y_l^m(\theta',\phi')\sin\theta'\,d\theta'\,d\phi'\,dr'\\&+\int_{r',\theta',\phi'}\mathbf{M}_\theta(\theta',\phi')\left[\frac{r'(\theta',\phi')}{r}\right]^{l+1}\frac{\partial Y_l^m(\theta',\phi')}{\partial\theta'}\sin\theta'\,d\theta'\,d\phi'\,dr'\\&+\int_{r',\theta',\phi'}\mathbf{M}_\phi(\theta',\phi')\left[\frac{r'(\theta',\phi')}{r}\right]^{l+1}\frac{\partial Y_l^m(\theta',\phi')}{\partial\phi'}\frac{1}{\sin\theta'}\sin\theta'\,d\theta'\,d\phi'\,dr'\Bigg\}\end{aligned} \tag{A4}$$

Integrating over the radial direction, we obtain

$$\begin{aligned}V(\mathbf{r})=\frac{\mu_0}{4\pi}\sum_l\sum_m Y_l^m(\theta,\phi)\,\frac{r}{l+2}\int_{\theta',\phi'}&\left[\left(\frac{r_2(\theta',\phi')}{r}\right)^{l+2}-\left(\frac{r_1(\theta',\phi')}{r}\right)^{l+2}\right]\cdot\\&\left[l\mathbf{M}_r\,Y_l^m(\theta',\phi')+\mathbf{M}_\theta\frac{\partial Y_l^m(\theta',\phi')}{\partial\theta'}+\mathbf{M}_\phi\frac{\partial Y_l^m(\theta',\phi')}{\partial\phi'}\frac{1}{\sin\theta'}\right]\sin\theta'\,d\theta'\,d\phi'.\end{aligned} \tag{A5}$$

The magnetic field $\mathbf{B}$ is the gradient of the magnetic potential V

$$\mathbf{B}=-\nabla V. \tag{A6}$$

Introducing Equation A5 into Equation A6, we obtain

$$\begin{aligned}\mathbf{B}(\mathbf{r})=\frac{\mu_0}{4\pi}\sum_l\sum_m&\left(Y_l^m(l+1)\,\hat{r}-\frac{\partial Y_l^m}{\partial\theta}\hat{\theta}-\frac{\partial Y_l^m}{\partial\phi}\frac{1}{\sin\theta}\hat{\phi}\right)\cdot\\&\frac{1}{l+2}\int_{\theta',\phi'}\left[\left(\frac{r_2}{r}\right)^{l+2}-\left(\frac{r_1}{r}\right)^{l+2}\right]\left(l\mathbf{M}_r\,Y_l^m+\mathbf{M}_\theta\frac{\partial Y_l^m}{\partial\theta'}+\mathbf{M}_\phi\frac{\partial Y_l^m}{\partial\phi'}\frac{1}{\sin\theta'}\right)\sin\theta'\,d\theta'\,d\phi'.\end{aligned} \tag{A7}$$

Data Availability Statement

Both the synthetic magnetic field observations (input) and inversion solution files (output) can be found in Zenodo repository (Oliveira & Vervelidou, 2024), as well as the inversion software (Oliveira, 2024). Inversion results for Reiner Gamma and Mendel-Rydberg are also available in the same repository. The lunar magnetic field map used for our inversions is from Tsunakawa et al. (2015). Maps from Figure 14 are built with GMT software (Wessel et al., 2019).

Acknowledgments
We would like to thank both the Editor and Associate Editor as well as two anonymous reviewers for their comments that helped to improve our manuscript. MDM is funded by the Spanish Program for Research, Development and Innovation under the project MINOTAUR of reference PID2020-119208RB-I00. JSO thanks insightful discussions with Dr. Thomas Cornet, Dr. Valentina Galluzzi and Dr. Emma Losantos. Joana S. Oliveira and Foteini Vervelidou are funded by the European Commission under the Marie Skłodowska-Curie Actions programme, with the grant agreements No. 893304 and No. 844252, respectively.

References

Arkani-Hamed, J., & Boutin, D. (2014). Analysis of isolated magnetic anomalies and magnetic signatures of impact craters: Evidence for a core dynamo in the early history of the Moon. *Icarus*, *237*, 262–277. https://doi.org/10.1016/j.icarus.2014.04.046

Bamford, R. A., Alves, E. P., Cruz, F., Kellett, B. J., Fonseca, R. A., Silva, L. O., et al. (2016). 3D PIC simulations of collisionless shocks at lunar magnetic anomalies and their role in forming lunar swirls. *The Astrophysical Journal*, *830*(2), 146. https://doi.org/10.3847/0004-637X/830/2/146

Blakely, R. J. (1996). *Potential theory in gravity and magnetic applications*. Cambridge University Press.

Blewett, D. T., Halekas, J., Ho, G. C., Greenhagen, B. T., Anderson, B. J., Vines, S. K., et al. (2022). Lunar Vertex: PRISM Exploration of Reiner Gamma. In *53rd Lunar and Planetary Science Conference* (Vol. 2678, p. 1131).

Carley, R. A., Whaler, K. A., Purucker, M. E., & Halekas, J. S. (2012). Magnetization of the lunar crust. *Journal of Geophysical Research*, *117*(E8), E08001. https://doi.org/10.1029/2011JE003944

Denevi, B. W., Robinson, M. S., Boyd, A. K., Blewett, D. T., & Klima, R. L. (2016). The distribution and extent of lunar swirls. *Icarus*, *273*, 53–67. https://doi.org/10.1016/j.icarus.2016.01.017

Dwyer, C. A., Stevenson, D. J., & Nimmo, F. (2011). A long-lived lunar dynamo driven by continuous mechanical stirring. *Nature*, *479*(7372), 212–214. https://doi.org/10.1038/nature10564

Fuller, M., & Cisowski, S. M. (1987). Lunar paleomagnetism. *Geomagnetism*, *2*, 307–455.

Galluzzi, V., Oliveira, J. S., Wright, J., Rothery, D. A., & Hood, L. L. (2021). Asymmetric magnetic anomalies over young impact craters on Mercury. *Geophysical Research Letters*, *48*(5), e2020GL091767. https://doi.org/10.1029/2020GL091767

Garrick-Bethell, I., Head, J. W., & Pieters, C. M. (2011). Spectral properties, magnetic fields, and dust transport at lunar swirls. *Icarus*, *212*(2), 480–492. https://doi.org/10.1016/j.icarus.2010.11.036

Garrick-Bethell, I., & Kelley, M. R. (2019). Reiner Gamma: A magnetized elliptical disk on the Moon. *Geophys. Res. Lett.*, *46*(10), 5065–5074. https://doi.org/10.1029/2019GL082427

Gong, S., & Wieczorek, M. A. (2020). Is the lunar magnetic field correlated with gravity or topography? *Journal of Geophysical Research: Planets*, *125*(4), e06274. https://doi.org/10.1029/2019JE006274

Gubbins, D., Ivers, D., Masterton, S. M., & Winch, D. E. (2011). Analysis of lithospheric magnetization in vector spherical harmonics. *Geophysical Journal International*, *187*(1), 99–117. https://doi.org/10.1111/j.1365-246x.2011.05153.x

Hemingway, D., & Garrick-Bethell, I. (2012). Magnetic field direction and lunar swirl morphology: Insights from Airy and Reiner Gamma. *Journal of Geophysical Research*, *117*(E10), E10012. https://doi.org/10.1029/2012JE004165

Hemingway, D. J., & Tikoo, S. M. (2018). Lunar swirl morphology constrains the geometry, magnetization, and origins of lunar magnetic anomalies. *Journal of Geophysical Research: Planets*, *123*(8), 2223–2241. https://doi.org/10.1029/2018JE005604

Hood, L. L. (2011). Central magnetic anomalies of Nectarian-aged lunar impact basins: Probable evidence for an early core dynamo. *Icarus*, *211*(2), 1109–1128. https://doi.org/10.1016/j.icarus.2010.08.012

Hood, L. L., & Artemieva, N. A. (2008). Antipodal effects of lunar basin-forming impacts: Initial 3D simulations and comparisons with observations. *Icarus*, *193*(2), 485–502. https://doi.org/10.1016/j.icarus.2007.08.023

Hood, L. L., Oliveira, J. S., Andrews-Hanna, J., Wieczorek, M. A., & Stewart, S. T. (2021). Magnetic anomalies in five lunar impact basins: Implications for impactor trajectories and inverse modeling. *Journal of Geophysical Research: Planets*, *126*(2), e2020JE006668. https://doi.org/10.1029/2020JE006668

Hood, L. L., Russell, C. T., & Coleman, P. J. (1981). Contour maps of lunar remanent magnetic fields. *Journal of Geophysical Research*, *86*(B2), 1055–1069. https://doi.org/10.1029/JB086iB02p01055

Hood, L. L., & Schubert, G. (1980). Lunar magnetic anomalies and surface optical properties. *Science*, *208*(4439), 49–51. https://doi.org/10.1126/science.208.4439.49

Hood, L. L., Torres, C. B., Oliveira, J. S., Wieczorek, M. A., & Stewart, S. T. (2021). A new large-scale map of the lunar crustal magnetic field and its interpretation. *Journal of Geophysical Research: Planets*, *126*(2), e2020JE006667. https://doi.org/10.1029/2020JE006667

Hood, L. L., & Williams, C. R. (1989). The lunar swirls: Distribution and possible origins. *Lunar and Planetary Science Conference Proceedings*, *19*, 99–113.

Hood, L. L., Zakharian, A., Halekas, J., Mitchell, D., Lin, R., Acuña, M., & Binder, A. (2001). Initial mapping and interpretation of lunar crustal magnetic anomalies using Lunar Prospector magnetometer data. *Journal of Geophysical Research*, *106*(E11), 27825–27839. https://doi.org/10.1029/2000je001366

Katanforoush, A., & Shahshahani, M. (2003). Distributing points on the sphere. *Exper. Math.*, *12*(2), 199–209. https://doi.org/10.1080/10586458.2003.10504492

Kelley, M. R., & Garrick-Bethell, I. (2020). Gravity constraints on the age and formation of the Moon's Reiner Gamma magnetic anomaly. *Icarus*, *338*, 113465. https://doi.org/10.1016/j.icarus.2019.113465

Laneuville, M., Taylor, J., & Wieczorek, M. A. (2018). Distribution of radioactive heat sources and thermal history of the moon. *Journal of Geophysical Research: Planets*, *123*(12), 3144–3166. https://doi.org/10.1029/2018JE005742

Laneuville, M., Wieczorek, M. A., Breuer, D., Aubert, J., Morard, G., & Rückriemen, T. (2014). A long-lived lunar dynamo powered by core crystallization. *Earth and Planetary Science Letters*, *401*, 251–260. https://doi.org/10.1016/j.epsl.2014.05.057

Lawson, C. L., & Hanson, R. J. (1974). *Solving least squares problems*. Prentice-Hall.

Le Bars, M., Wieczorek, M. A., Karatekin, Ö., Cébron, D., & Laneuville, M. (2011). An impact-driven dynamo for the early Moon. *Nature*, *479*(7372), 215–218. https://doi.org/10.1038/nature10565

Lin, R. P. (1979). High spatial resolution measurements of surface magnetic fields of the lunar frontside. In N. W. Hinners (Ed.), *Proceedings of the Lunar and Planetary Science Conference* (Vol. 10, pp. 2259–2264).

Maxwell, R. E., & Garrick-Bethell, I. (2020). Evidence for an ancient near-equatorial lunar dipole from higher precision inversions of crustal magnetization. *Journal of Geophysical Research: Planets*, *125*(12), e06567. https://doi.org/10.1029/2020JE006567

Mitchell, D., Halekas, J., Lin, R., Frey, S., Hood, L., Acuña, M. H., & Binder, A. (2008). Global mapping of lunar crustal magnetic fields by lunar prospector. *Icarus*, *194*(2), 401–409. https://doi.org/10.1016/j.icarus.2007.10.027

Nayak, M., Hemingway, D., & Garrick-Bethell, I. (2017). Magnetization in the South Pole-Aitken basin: Implications for the lunar dynamo and true polar wander. *Icarus*, *286*, 153–192. https://doi.org/10.1016/j.icarus.2016.09.038

Neumann, G. A., Zuber, M. T., Wieczorek, M. A., Head, J. W., Baker, D. M. H., Solomon, S. C., et al. (2015). Lunar impact basins revealed by Gravity Recovery and Interior Laboratory measurements. *Sciences Advances*, *1*(9), e1500852. https://doi.org/10.1126/sciadv.1500852

Nicholas, J. B., Purucker, M. E., & Sabaka, T. J. (2007). Age spot or youthful marking: Origin of Reiner Gamma. *Geophysical Research Letters*, *34*(2), L02205. https://doi.org/10.1029/2006GL027794

Oliveira, J. S. (2024). Software for lunar crustal magnetic sources distribution (Version v1). Zenodo. https://doi.org/10.5281/zenodo.10653723
Oliveira, J. S., Hood, L. L., & Langlais, B. (2019). Constraining the early history of Mercury and its core dynamo by studying the crustal magnetic field. *Journal of Geophysical Research: Planets*, *124*(9), 2382–2396. https://doi.org/10.1029/2019JE005938
Oliveira, J. S., & Vervelidou, F. (2024). Dataset for lunar crustal magnetic sources distribution (Version v2) [Dataset]. Zenodo. https://doi.org/10.5281/zenodo.10655201
Oliveira, J. S., & Wieczorek, M. A. (2017). Testing the axial dipole hypothesis for the Moon by modeling the direction of crustal magnetization. *Journal of Geophysical Research: Planets*, *122*(2), 383–399. https://doi.org/10.1002/2016JE005199
Oliveira, J. S., Wieczorek, M. A., & Kletetschka, G. (2017). Iron abundances in lunar impact basin melt sheets from orbital magnetic field data. *Journal of Geophysical Research: Planets*, *122*(12), 2429–2444. https://doi.org/10.1002/2017JE005397
Oran, R., Weiss, B. P., Shprits, Y., Miljković, K., & Tóth, G. (2020). Was the Moon magnetized by impact plasmas? *Science Advances*, *6*(40), eabb1475. https://doi.org/10.1126/sciadv.abb1475
Parker, R. L. (1991). A theory of ideal bodies for seamount magnetism. *Journal of Geophysical Research*, *96*(B10), 16101–16112. https://doi.org/10.1029/91JB01497
Purucker, M. E. (2008). A global model of the internal magnetic field of the moon based on lunar prospector magnetometer observations. *Icarus*, *197*(1), 19–23. https://doi.org/10.1016/j.icarus.2008.03.016
Purucker, M. E., Head, III, J. W., & Wilson, L. (2012). Magnetic signature of the lunar South Pole-Aitken basin: Character, origin, and age. *Journal of Geophysical Research*, *117*(E5), E05001. https://doi.org/10.1029/2011JE003922
Purucker, M. E., & Nicholas, J. B. (2010). Global spherical harmonic models of the internal magnetic field of the Moon based on sequential and coestimation approaches. *Journal of Geophysical Research*, *115*(E12), E12007. https://doi.org/10.1029/2010JE003650
Richmond, N. C., & Hood, L. L. (2008). A preliminary global map of the vector lunar crustal magnetic field based on Lunar Prospector magnetometer data. *Journal of Geophysical Research*, *113*(E2), E02010. https://doi.org/10.1029/2007JE002933
Scheinberg, A., Soderlund, K. M., & Schubert, G. (2015). Magnetic field generation in the lunar core: The role of inner core growth. *Icarus*, *254*, 62–71. https://doi.org/10.1016/j.icarus.2015.03.013
Takahashi, F., Tsunakawa, H., Shimizu, H., Shibuya, H., & Matsushima, M. (2014). Reorientation of the early lunar pole. *Nature Geosci*, *7*(6), 409–412. https://doi.org/10.1038/ngeo2150
Tarduno, J. A., Cottrell, R. D., Lawrence, K., Bono, R. K., Huang, W., Johnson, C. L., et al. (2021). Absence of a long-lived lunar paleomagnetosphere. *Science Advances*, *7*(32), eabi7647. https://doi.org/10.1126/sciadv.abi7647
Thomas, P., Grott, M., Morschhauser, A., & Vervelidou, F. (2018). Paleopole reconstruction of Martian magnetic field anomalies. *Journal of Geophysical Research: Planets*, *123*(5), 1140–1155. https://doi.org/10.1002/2017JE005511
Tsunakawa, H., Shibuya, H., Takahashi, F., Shimizu, H., Matsushima, M., Matsuoka, A., et al. (2010). Lunar magnetic field observation and initial global mapping of lunar magnetic anomalies by MAP-LMAG onboard SELENE (Kaguya). *Space Science Reviews*, *154*(1–4), 219–251. https://doi.org/10.1007/s11214-010-9652-0
Tsunakawa, H., Takahashi, F., Shimizu, H., Shibuya, H., & Matsushima, M. (2015). Surface vector mapping of magnetic anomalies over the Moon using Kaguya and Lunar Prospector observations. *Journal of Geophysical Research: Planets*, *120*(6), 1160–1185. https://doi.org/10.1002/2014JE004785
Vaughan, W. M., Head, J. W., Wilson, L., & Hess, P. C. (2013). Geology and petrology of enormous volumes of impact melt on the Moon: A case study of the Orientale basin impact melt sea. *Icarus*, *223*(2), 749–765. https://doi.org/10.1016/j.icarus.2013.01.017
Wessel, P., Luis, J. F., Uieda, L., Scharroo, R., Wobbe, F., Smith, W. H. F., & Tian, D. (2019). The generic mapping tools version 6. *Geochemistry, Geophysics, Geosystems*, *20*(11), 5556–5564. https://doi.org/10.1029/2019GC008515
Wieczorek, M. A. (2018). Strength, depth, and geometry of magnetic sources in the crust of the Moon from localized power spectrum analysis. *Journal of Geophysical Research: Planets*, *123*(1), 291–316. https://doi.org/10.1002/2017JE005418
Wieczorek, M. A., Weiss, B. P., Breuer, D., Cébron, D., Fuller, M., Garrick-Bethell, I., et al. (2022). Lunar magnetism. Retrieved from https://hal.science/hal-03524536
Wieczorek, M. A., Weiss, B. P., & Stewart, S. T. (2012). An impactor origin for lunar magnetic anomalies. *Science*, *335*(6073), 1212–1215. https://doi.org/10.1126/science.1214773